Research paper

Effect of pulsating flow on flow-induced vibrations of circular and square cylinders in the laminar regime

Xinyu Wang [a,b], Zhongliang Zhang [a,b], Kai Shi [a], Xuefeng Zhu [a], Xu Guo [a,b,c], Yue Mei [a,b,c,**], Chennakesava Kadapa [d,*]

[a] *Department of Engineering Mechanics, Dalian University of Technology, Dalian, 116024, China*
[b] *State Key Laboratory of Structural Analysis for Industrial Equipment, Department of Engineering Mechanics, Dalian University of Technology, Dalian, 116023, China*
[c] *Ningbo Institute of Dalian University of Technology, Ningbo, China*
[d] *School of Computing, Engineering and the Built Environment, Edinburgh Napier University, Edinburgh, EH10 5DT, United Kingdom*

A B S T R A C T

Through fluid-structure interaction simulations, this study assesses the dynamic response characteristics of elastically mounted circular and square cylinders subjected to pulsating inflow conditions, providing valuable insights into the analysis and optimization of these systems. The main focus of the present work is on analyzing the effects of two factors: (i) the ratio of the oscillatory velocity component to the steady velocity component in pulsating flow (flow ratio) and (ii) the ratio of the oscillation frequency of pulsating flow to the natural frequency of the structure (frequency ratio). The simulation results for different parameters of interest are analysed using Fourier analysis and Poincaré maps of time series data, and contour plots of vorticity. For the circular cylinder, it is found that cylinder loses synchronization in lock-in as the flow and frequency ratios are increased. Three distinct vibration patterns of vortex-induced vibration are observed for selected combinations of flow and frequency ratios at a Reynolds number of 110 for circular cylinder. For the galloping of square cylinder at a Reynolds number of 250, it is found that the instability and nonlinearity of vortex shedding become more pronounced as the flow ratio increases.

1. Introduction

Flow-induced vibration (FIV) of bluff bodies is a phenomenon that has significant implications for a variety of problems in science and engineering, such as offshore platforms and bridge cables (Jafari et al., 2020), heat exchangers (Weaver and Fitzpatrick, 1988), power generation (including piezoelectric generators and energy harvester (Zhang et al., 2021)) and oil and gas industry, specifically pipelines. The dynamic behavior of FIV is complex and highly dependent on the characteristics of both the fluid and the structure. To develop a thorough understanding of FIV, extensive research has been conducted to investigate the fundamental mechanisms and suppression strategies of FIV. Since the literature on FIV phenomenon is vast, we present the literature that is closely relevant to the present work. Li et al. (2011) employed unsteady Navier–Stokes equations to study the vortex-induced vibrations (VIVs) of circular cylinders at very low Reynolds numbers to find the fundamental mechanisms of the VIV. Bokaian and Geoola (1984)

observed the coexistence of VIV and galloping. The effect of vortices generated by a rigidly mounted cylinder on the fluttering response of an airfoil is investigated by Derakhshandeh et al. (2016). Menon and Mittal (2019) presented a computational study of the dynamics of flow-induced pitch oscillations in an airfoil, exploring the effects of various parameters on the dynamics of flutter. Wang et al. (2023) explored the suppression effect of FIV caused by symmetrically installed groove structures with different shapes under high Reynolds numbers and provides valuable insights for the design and optimization of energy harvesting technologies in marine engineering. Tian et al. (2023a) proposed a novel magnetically-coupled airfoil-based flutter piezoelectric energy harvester to achieve enhanced energy harvesting performance, which establishes a foundation for the practical application of a magnetically-coupled leaf-shaped fluttering piezoelectric energy harvester in low wind-speed environments. An innovative approach, involving the adjustment of trailing-edge flap installation angles, was introduced by Tian et al. (2023b) to enhance the performance of

piezoelectric energy harvesting devices, which has been demonstrated as providing guidance for achieving a balance between energy harvesting and vibration suppression by both experimental and numerical simulations.

FIV in circular cylinders is typically referred to as VIV because it arises from the shedding of vortices. VIV of a circular cylinder is a self-limiting motion induced by vortex shedding, which can cause fatigue damage to the structures due to the periodic oscillations of higher-amplitude in the "lock-in" regime. Extensive fundamental research has been conducted to better understand the coupling between the motion of an elastically mounted cylinder and the dynamics of the wake, which includes the alternate shedding of vortices that generate and interact with the VIV of the cylinder. A significant number of experimental studies have been conducted on the VIV of a circular cylinder, with Bearman (1984), Williamson et al. (Jauvtis and Williamson, 2004; Williamson and Govardhan, 2008) and Sarpkaya (2004) providing comprehensive reviews of fundamental concepts on VIV. Recently, data-driven methods have emerged as useful and efficient approaches for predicting the response of VIV. For example, Gao et al. (2023) introduced a data-driven and knowledge-enhanced semi-empirical modeling approach, achieving precise prediction of nonlinear vortex-induced vibration phenomena through the modification of a typical oscillator model. These simulations have helped identify ranges of several important dimensionless parameters that influence VIV response, including mass ratio (Khalak and Williamson, 1997; Prasanth and Mittal, 2008; Qiu et al., 2021), structural damping ratio (Martins and Avila, 2019; Qi et al., 2023), and Reynolds number (Zhao et al., 2014). Nevertheless, it should be noted that the majority of research has been limited to investigating the VIV of circular cylinders against constant inflow. However, in more realistic conditions, fluid velocity is rarely a constant, for example, when studying hydrodynamics around structures. In the literature, only a few studies have been carried out on VIV against pulsating inflow compared to constant inflow conditions. Bearman (Bearman et al., 1985) and An et al. (2009) demonstrated that the number of vortices shed from the cylinder is directly related to the period of the oscillatory flow. Anagnostopoulos and Iliadis (1998) conducted a numerical study on VIV of a circular cylinder and found that the response of the cylinder was significantly amplified when the oscillatory flow frequency was close to the natural frequency of the cylinder. Zhao et al. (2012) conducted simulations on the transverse vibration of VIV of a cylinder in oscillatory flows at different periods and flow velocities of the oscillatory flow, revealing that the response of the cylinder had more than one frequency component as the reduced velocity increased. More recently, Zhao et al. (2013) investigated VIV of a circular cylinder in combined steady and oscillatory flows at different flow ratios, and found that the combination of steady and oscillatory flow can widen the lock-in regime.

Galloping of a square cylinder is another important mechanism of FIV that differs from VIV in its cause. Galloping is a self-excited instability that leads to high-amplitude and low-frequency oscillations in lightly damped structures with a bluff frontal geometry (Daqaq et al., 2022). A large body of theoretical and experimental work has been conducted on transverse galloping, which has been reviewed in Parkinson (1974) and Blevins (1990). Bearman et al. (1987) conducted an experimental study of the FIV of a square cylinder in a wind tunnel. Parkinson and Smith (1964) predicted transverse galloping of a square cylinder by quasi-steady theory and obtained critical velocities that were in good agreement with experimental data. This model has since been widely used by Kazakevich et al. (Kazakevich and Vasilenko, 1996) and Alonso et al. (Alonso and Meseguer, 2006) to investigate the effects of various physical parameters on the behavior of the galloping in different structures. Joly et al. (2012) developed a quasi-steady model to study the galloping of a square cylinders at low Reynolds numbers. Luo et al. (2003) investigated the flow around a stationary square cylinder at different angles of attack and Reynolds numbers, exploring the reasons behind the hysteresis phenomena in the flow. Han and Langre (Han and

de Langre, 2022) proposes a reduced-order model (ROM) to characterize galloping of a square cylinder, which has been demonstrated that the model can partially quantitatively reproduce the galloping behavior of the square cylinder under low Reynolds numbers and low mass ratios. In recent years, several studies have focused on the passive energy sink (Guo et al., 2017; Modi et al., 1995) to suppress galloping oscillations. Abdelkefi et al. (2012) and Andrianne et al. (2018) have investigated the possibility of designing enhanced piezoelectric energy harvesters that exploit the galloping of square cylinders. While numerous studies have been focused on the occurrence and suppression of galloping or exploiting for energy harvesting, to the best of authors' knowledge, there are no studies on the response characteristics of galloping in pulsating inflow conditions.

It is important to note that the current literature on FIV of cylindrical structures in pulsating flow has primarily focused on the influence of flow ratios between oscillatory and steady flows on VIV at a fixed Keulegan–Carpenter (KC) number. However, in this paper, we focus on lock-in of a circular cylinder and galloping of a square cylinder in the laminar flow regime and under pulsating inflow conditions for the first time. We investigate dynamic response of circular and square structures in pulsating flow using high-fidelity fluid-structure interaction (FSI) simulations, taking into consideration the influences of both the amplitude of pulsating flow from the mean value (a) and the frequency ratio (f_p/f_n) between the frequency of pulsating flow (f_p) and the natural frequency of the structure (f_n) on the response characteristics. The main contribution of this work is: (i) computational studies of the effect of pulsating flow on the dynamic response of elastically mounted circular and square cylinders for different parameters of the pulsating inflow velocity and (ii) investigation of the effect of pulsating inflow velocity on the lock-in of a circular cylinder and galloping of a square body.

The remainder of this paper is organized as follows. In Section 2, we describe the problems of interests and briefly discuss the simulation framework used for FSI simulations in this work. In Section 3.1, we discuss the van der Pol oscillator and its validations. In Section 3.2, we compare our FSI simulation results with those of other numerical investigations available in the literature to verify our numerical scheme. We also use nonlinear dynamic tools to characterize VIV regimes of the circular cylinder in pulsating flow. In Section 4.1, we present the quasi-steady theory and validations of the square cylinder. We compare our FSI simulation results of galloping in uniform flow with those of other research works, and illustrate the dynamic behaviors of galloping of the square cylinder under pulsating flow in Section 4.2. Finally, we present our conclusions and discussions in Section 5.

2. Problem description and numerical method

To explore the mechanical response of the rigid body under pulsating inflow, we study two physical models. The first model is the VIV of a circular cylinder, and the second model is galloping of a square cylinder.

For the circular cylinder model, we establish the model of a two-dimensional circular cylinder with a transverse degree of freedom, which is depicted in Fig. 1(a). A circular cylinder with a diameter of D = 1 cm is initially located at $(20\text{cm}, 20\text{cm})$ in a fluid domain with a size of 60×40 cm^2. The velocity at the inlet is $U = U_0 \quad [1 + a\sin(\omega_p t)]$, where U_0 is the mean (steady) inlet velocity, a is the amplitude of pulsating flow about the mean velocity, and $\omega_p = 2\pi f_p$ with f_p as the frequency of pulsating flow. In this work, the density of the fluid is $\rho^f = 1$ g cm^{-3} and its viscosity is $\mu^f = 0.01$ g cm^{-1}s^{-1}. Mechanical properties of the solid model are given by: $m^s = 117.10$ g, $k^s = 184.9169081$ g s^{-2} and $c^s = 0.35317$ g s^{-1}, leading to the mass ratio, $m^* = m^s/m^f = 149.1$, the damping ratio, $\xi = 0.0012$, and the natural frequency, $f_n = 0.2$ Hz.

For the square cylinder model as shown in Fig. 1(b), the size of the domain and properties of the fluid are the same as that of the circular cylinder model. The pulsating velocity $U = U_0 \quad [1 + a\sin(\omega_p t)]$ is imposed at the inlet in X-direction and $U_0 = 2.5$ cm s^{-1} so that the
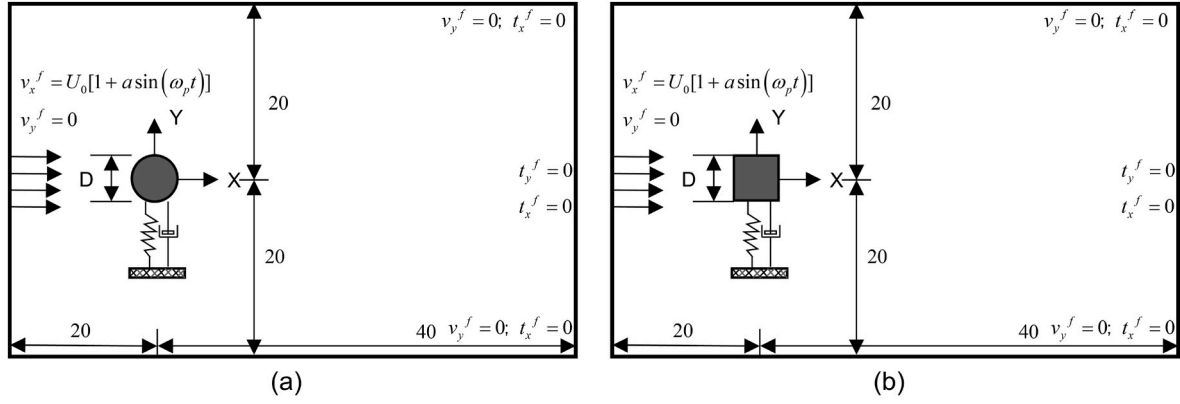
Fig. 1. The geometry and boundary condition: (a) Flow past the circular cylinder, (b) Flow past the square cylinder.

Reynolds number is $\rho D U_0 / \mu = 250$. The mass, damping and stiffness of the square cylinder are given by: $m^s = 20$ g, $k^s = 3.08425$ g s^{-2} and $c^s = 0.0581195$ g s^{-1}, leading to the mass ratio, $m^* = m^s / m^f = 20$, the damping ratio, $\xi = 0.0037$, and the natural frequency, $f_n = 0.0625$ Hz.

The fluid flow is assumed to be isothermal and incompressible. For the range of Reynolds numbers considered, the flow is laminar. To simulate the FSI problems, we adopt the stabilized immersed computational framework proposed in (Dettmer et al., 2016; Kadapa et al., 2017). In this framework, the fluid problem is solved by the CutFEM (Burman et al., 2015). The fluid domain is discretized with hierarchical B-splines (Bornemann and Cirak, 2013; Rüberg and Cirak, 2014) with fixed Cartesian grids. The Navier-Stokes equations are solved by using the SUPG/PSPG finite element formulation (Tezduyar et al., 1992; Tezduyar and Senga, 2006). For the detailed discussion of the formulations, the reader is referred to (Kadapa et al., 2017, 2018).

The equation for the dynamics of rigid solids is given by

$$\mathbf{M}\mathbf{a}^s + \mathbf{C}\mathbf{v}^s + \mathbf{K}\mathbf{d}^s = \mathbf{F}^s \tag{1}$$

where $\mathbf{d}^s$, $\mathbf{v}^s$ and $\mathbf{a}^s$ are the displacement, velocity and acceleration vectors of the rigid body, respectively, and $\mathbf{F}^s$ is the force acting on the rigid body. $\mathbf{M}$, $\mathbf{C}$ and $\mathbf{K}$ are mass, damping and stiffness matrices, respectively.

The FSI coupling is solved by a second-order accurate staggered numerical scheme (Dettmer et al., 2021; Dettmer and Perić, 2013; Kadapa et al., 2022), which is demonstrated to be computationally efficient, robust, and capable of handling FSI problems with mass ratios as low as 0.01 (Kadapa et al., 2017). This scheme is based on the second-order temporal accuracy of generalized-α method (Jansen et al., 2000). In this coupling scheme, both the fluid and solid problems are solved only once at every time step. The flowchart of the FSI solver is shown in Fig. 2. The parameter β $(0 < \beta \leq 1)$ in Fig. 2 is defined as the relaxation factor (Dettmer and Perić, 2013). The critical value of β is primarily determined by the mass ratio, and it influences the stability of the staggered scheme. Further details of the coupling scheme can be found in (Dettmer et al., 2021; Kadapa et al., 2020). From the numerical examples in (Dettmer et al., 2021; Kadapa, 2020), we observed that the adapted FSI solver yields accurate results without the need for many time steps per one time period.

The finite element mesh utilized for the simulations is depicted in Fig. 3. Starting with a 119×91 element grid, the mesh is refined locally up to three levels in the proximity of the cylinder. Consequently, the coarsest element size measures 0.50420 cm $\times$ 0.49383 cm, while the finest element size measures 0.06303 cm $\times$ 0.06173 cm. The zoomed views of Fig. 3(a) and (b) display the sub triangulations of cut elements for the circular cylinder and square cylinder, respectively. In the simulations involving the circular cylinder, a constant uniform time step of
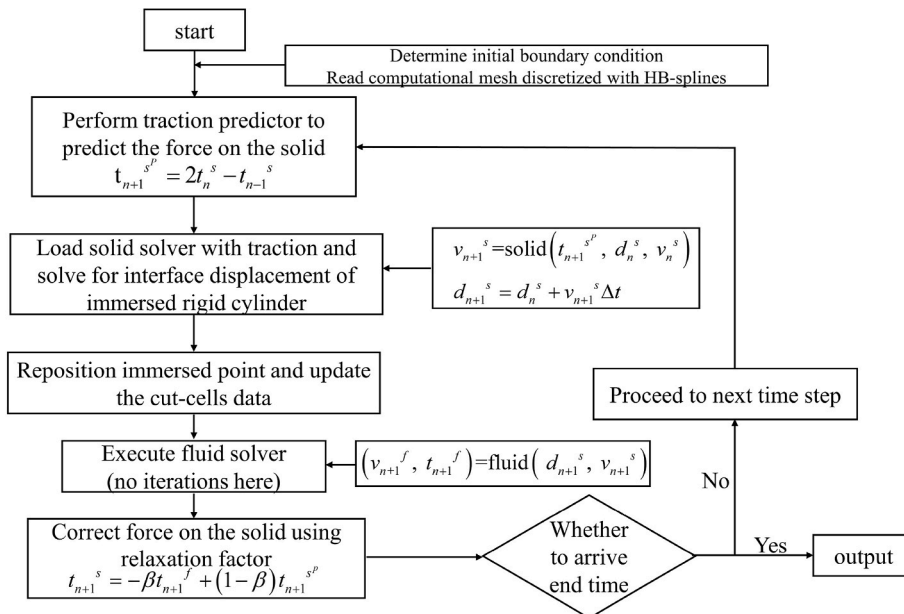
Fig. 2. The flowchart of the FSI solver used in this paper.
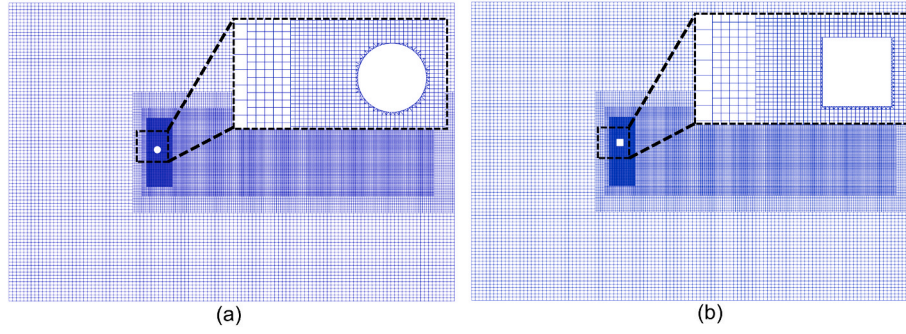
Fig. 3. The finite element mesh used for the simulations: (a) Flow past the circular cylinder, (b) Flow past the square cylinder.

$\Delta t = 0.1$ s is employed. On the other hand, a time step of $\Delta t = 0.05$ s is used for all simulations concerning the square cylinder. Before conducting the vibration response simulations, both spatial and temporal convergence are evaluated. To assess convergence, unsteady flow past fixed circular and square cylinders for Reynolds numbers of 100 and 200, as well as lock-in of circular cylinder and translational galloping of a square cylinder at low Reynolds numbers, were considered. Convergence studies and our previous experience show that three levels of refinement and the chosen time step sizes yield accurate results for lock-in and galloping problems in the laminar regime. For more comprehensive information regarding the convergence study for these problems, reader is referred to (Dettmer et al., 2021; Kadapa, 2020).

3. Lock-in of a circular cylinder

3.1. Mathematical model of VIV

The equation of motion for a circular cylinder supported on a spring and damper is given by

$$m\ddot{y} + c\dot{y} + ky = F_L(t) \tag{2}$$

where y is the displacement of the cylinder in vertical direction; k is the stiffness of the spring and, c is the damping coefficient. F_L is the force per unit length of the cylinder in the transverse direction, $F_L = \rho^f \ U^2 \ D \ C_f/2$. Note that, here $U = U_0 \ [1 + a\sin(\omega_p t)]$. The mass m is the combination of the mass of the structure m^s and the fluid-added mass m^f, which can be calculated from the following expression

$$m = m^s + m^f, m^f = \rho D^2 \pi / 4, \mu = (m^s + m^f) / \rho D^2 \tag{3}$$

where μ is a dimensionless mass ratio, and the linear damping in Eq. (2) $c = c^s + c^f$, where $c^f = \gamma \omega_s \rho D^2$. ω_s is the vortex shedding frequency which is given by $\omega_s = 2\pi St U/D$. St is the Strouhal number. γ is stall parameter which is a function of mean drag coefficient (Skop and Balasubramanian, 1997) and is fixed to 0.8 in this work.

In this work, VIV is modeled by the wake oscillator model, in which a nonlinear oscillator equation is introduced to model the oscillating lift force, arriving at the following van der Pol equation (Facchinetti et al., 2004)

$$\ddot{q} + \lambda \omega_s (q^2 - 1)\dot{q} + \omega_s^2 q = F \tag{4}$$

where, q is associated to the fluctuating lift coefficient on the structure, which describes the behavior of the near wake. λ is an empirical coefficient that should be determined by experimental results. In this paper, $\lambda = 0.55$ (Armin et al., 2018). F is the coupling term describing interaction between fluid and structure.

For the sake of convenience, we introduce dimensionless time and space coordinates, $\tau = \omega_s T$ and $Y = y/D$, respectively. In this case, Eq. (2) and Eq. (4) can be rewritten as

$$\ddot{Y} + \left(2\xi\delta + \frac{\gamma}{\mu}\right)\dot{Y} + \delta^2 Y = Mq, \ddot{q} + \lambda(q^2 - 1)\dot{q} + q = A\ddot{Y} \tag{5}$$

where $\xi = c^s/(2m\omega_n)$ is the structural damping ratio. $\delta = \omega_n/\omega_s$ denotes the reduced angular frequency of the structure where $\omega_n = \sqrt{k/m}$ is the circular natural frequency. $M = C_{L0}(1 + a\sin\omega_p t)^2/16\pi^2 St^2 \mu$ is the parameter which scales the effect of the wake on the structure, where C_{L0} is selected to 0.3 based on the observation on the experiments on the vortex shedding of a stationary circular cylinder. $A = 20$ based on the experimental results on lock-in in the literature (Plaschko, 2000).

In order to gain a comprehensive understanding of the mechanical behavior of VIV in relation to pulsating inflow parameters such as amplitude a and reduced frequency ratio f_p/f_n, it is crucial to validate the feasibility of FSI coupling scheme for VIV. This validation serves as a preliminary step in ensuring the accuracy and reliability of the coupled simulation approach when investigating VIV phenomena within the desired parameter range. We firstly consider the steady flow of the circular cylinder with a uniform free-stream velocity U_0, In this case, Eq. (5) can be solved by the time-accurate marching scheme (Cavaglieri and Bewley, 2015). The initial conditions are given by $y = \dot{y} = \dot{q} = 0, q$ is set to 0.000001 to introduce initial disturbance. When comparing the numerical results of the wake oscillator model, it is observed that the transverse displacement increases monotonically until the amplitude plateaus, as shown in Fig. 4(a). Slight difference in the amplitude of oscillations is attributed to the nonlinearities and the effect of parameters. The phase portrait displayed in Fig. 4(b) provides additional confirmation that the cylinder undergoes a periodic oscillation controlled by a limit cycle.

3.2. FSI simulation results and validation

To characterize the mechanical response of this oscillating system with varying a and f_p/f_n, we first perform simulations of the circular cylinder system with the constant inflow and compare the results with the literature (Dettmer and Perić, 2006; Kadapa, 2022). Fig. 5(a) shows that the normalized displacement amplitudes from the FSI simulations are in good agreement with reference values. It can be observed from Fig. 5(b) that, in the 'lock-in' regime (between $Re = 110$ and $Re = 120$), the ratio of vortex shedding frequency (f_s) and the natural frequency of the structure (f_n) is one. Moreover, beyond the lock-in regime, the values of frequency obtained using the present framework fit well with the Roshko's formula (Roshko, 1952) $f_s = U_0/D(0.212 - 4.5/Re)$. The "lock in" range of Re predicted by FSI simulation is narrower than that observed with the wake oscillator model. This difference is attributed to the fact that there are few empirical parameters chosen for the van der Pol oscillator model. Overall, the results obtained from the case of circular cylinder system under constant inflow illustrate that the chosen mesh and time step sizes yield results of sufficient accuracy.

Remark: We chose to present the results in Fig. 5 with respect to Reynolds number (Re) rather than the reduced velocity (U_r) because U_r
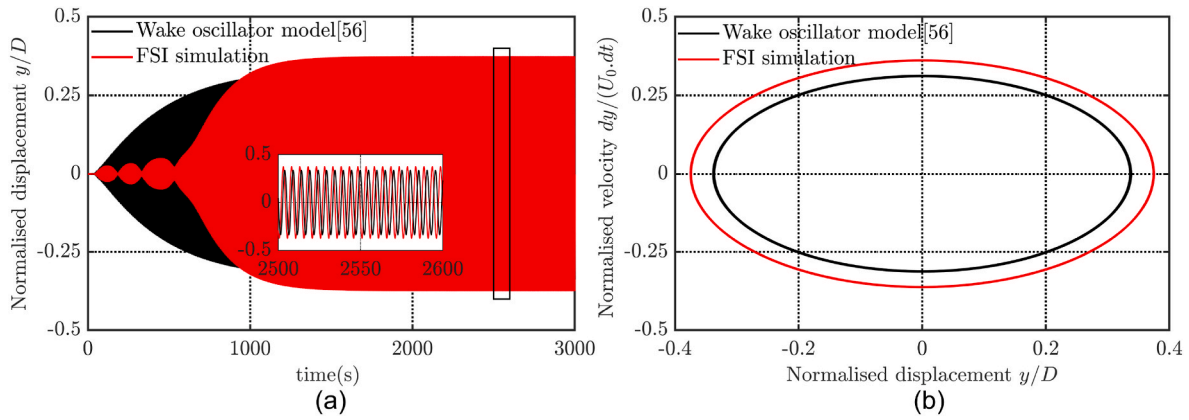
Fig. 4. Comparison of the dynamic behavior predicted by FSI simulation and the wake oscillator model at $Re = 110$: (a) displacement versus time, (b) phase portrait.
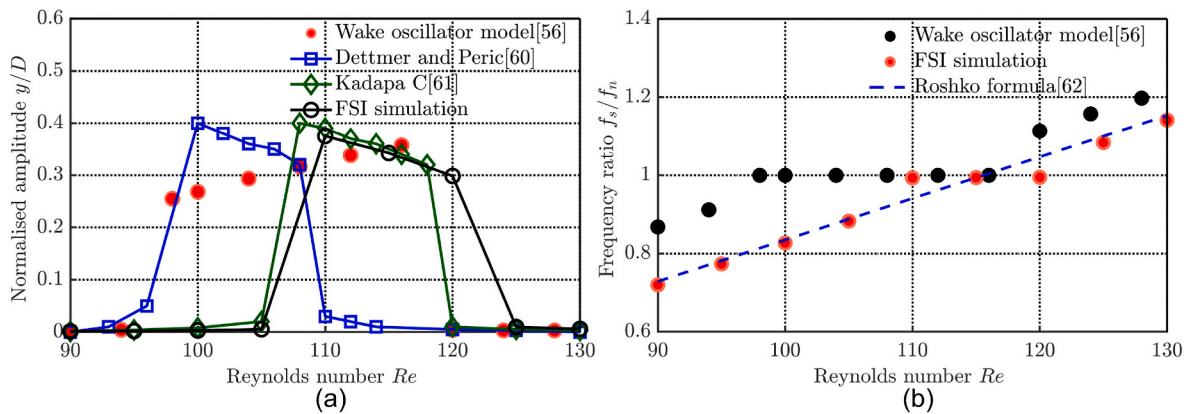
Fig. 5. Comparison of the cylinder using present FSI framework with simulation results from the literature:(a) non-dimensional amplitude, and (b) frequency ratio.

and Re are scalar multiples of each other since the structural frequency (f_n) is fixed. The response of the cylinder would be the same, except that the X-axis is scaled if presented in terms of U_r. From a practical viewpoint, changing the inflow velocity, hence Re, makes more sense. As Re is increased, shedding frequency (f_s) increases and the cylinder *locks-in,* once resonance ensues. For Re beyond lock-in zone, f_s increases further, in accordance with the Roshko's formula.

To investigate the dynamic behavior of the circular cylinder system under pulsating flow, we perform numerical simulations by varying a from 0.1 to 0.5 and f_p/f_n from 0.5 to 1.5 at $Re = 110$, which is the case with highest amplitude within the synchronization regime. We characterize the dynamic response of the system by using frequency spectra, phase portrait and Poincaré maps, as shown in Figs. 6–10. We observe that the amplitude of the cylinder with $a = 0.1$ is of the same order with the diameter of the cylinder as shown in Fig. 6(a), (e) and (i). This phenomenon can be better explained by observing the frequency spectra (see Fig. 6(b), (f) and (j)), where both the dominant vortex shedding frequency f_s and the oscillation frequency f_o are close to the structural natural frequency. The phase portraits (see Fig. 6(c), (g) and (k)) are single closed curves which demonstrate that the cylinder is in a steady-state vibration which controlled by the limit cycle. The associated Poincaré maps (see Fig. 6(d), (h) and (l)) consist of a single point, demonstrating that the mechanical response of this coupled system is periodic and harmonic for $a = 0.1$.

In the case of $a = 0.2$, we observe that the amplitude decreases when the frequency ratio is increased to 1.0 (see Fig. 7 (e)). Beating is the phenomenon found at $f_p/f_n = 1.0$ and 1.5 (see Fig. 7(e) and (i)). It is believed that the beating occurs because the inflow velocity increases and decreases periodically. Additionally, it is observed that multiple frequencies around the vortex shedding frequency appear for C_f. This

reveals that the vibration of the circular cylinder system is close to the bifurcation of the synchronization regime (see Fig. 7(f)). From Fig. 7(j), we observe that the vibration of the cylinder and the lift-force oscillate with different frequencies. It is apparent that the amplitude is lower than that presented in Fig. 7(e) as the frequency is increased to 1.5 (see Fig. 7 (i)). This validates that the cylinder is outside the synchronization regime. Further, the Poincaré maps indicate that the mechanical response of this system is quasi-periodic (see Fig. 7(h) and (l)).

Subsequently, we consider the motion of this system when a keeps increasing up to 0.5. We observe that the oscillation of the cylinder system is periodic, which is still within the 'lock-in' regime when $f_p/f_n = 0.5$ (see Fig. 8(a)–(d)). We observe the "beating" phenomenon when $f_p/f_n = 1.0$ as a is increased to 0.3 and 0.4 (see Figs. 8(e) and Fig. 9(e)). The periodic variation of the inlet velocity allows the change in vibration mode of the circular cylinder, which leads to the beating in the response. For $a = 0.4$ and 0.5, the amplitude is close to that obtained with $a = 0.3$ when $f_p/f_n = 0.5$ (see Figs. 9(a) and Fig. 10(a)). Moreover, the response is periodic (see Figs. 9(d) and Fig. 10(d)). However, it should be noted that the cylinder oscillates around $f_n = 0.2$ Hz, but the vortex shedding frequency is close to 0.3 Hz. Thus, it seems that the frequency $f = 0.2$ Hz of C_f is obtained by phase superposition of f_p and f_s (see Figs. 9(b) and Fig. 10(b)). The oscillation frequency f_o is close to shedding frequency f_s but far from the natural frequency f_n when $f_p/f_n = 1.0$ or 1.5 (see Figs. 8(f), (j), 9 (f), (j) and 10(j)). Thus, it can be inferred that the effect of nonlinearity on this system will be significantly amplified as a and f_p/f_n increase, which further induces the difference between f_o and f_n. There is a multi-loop limit cycle due to the existence of subharmonics (see Figs. 9(f), (g) and 10(f), (g)). The fact that the points in the Poincaré section display some periodic tendencies (see Figs. 9(h)
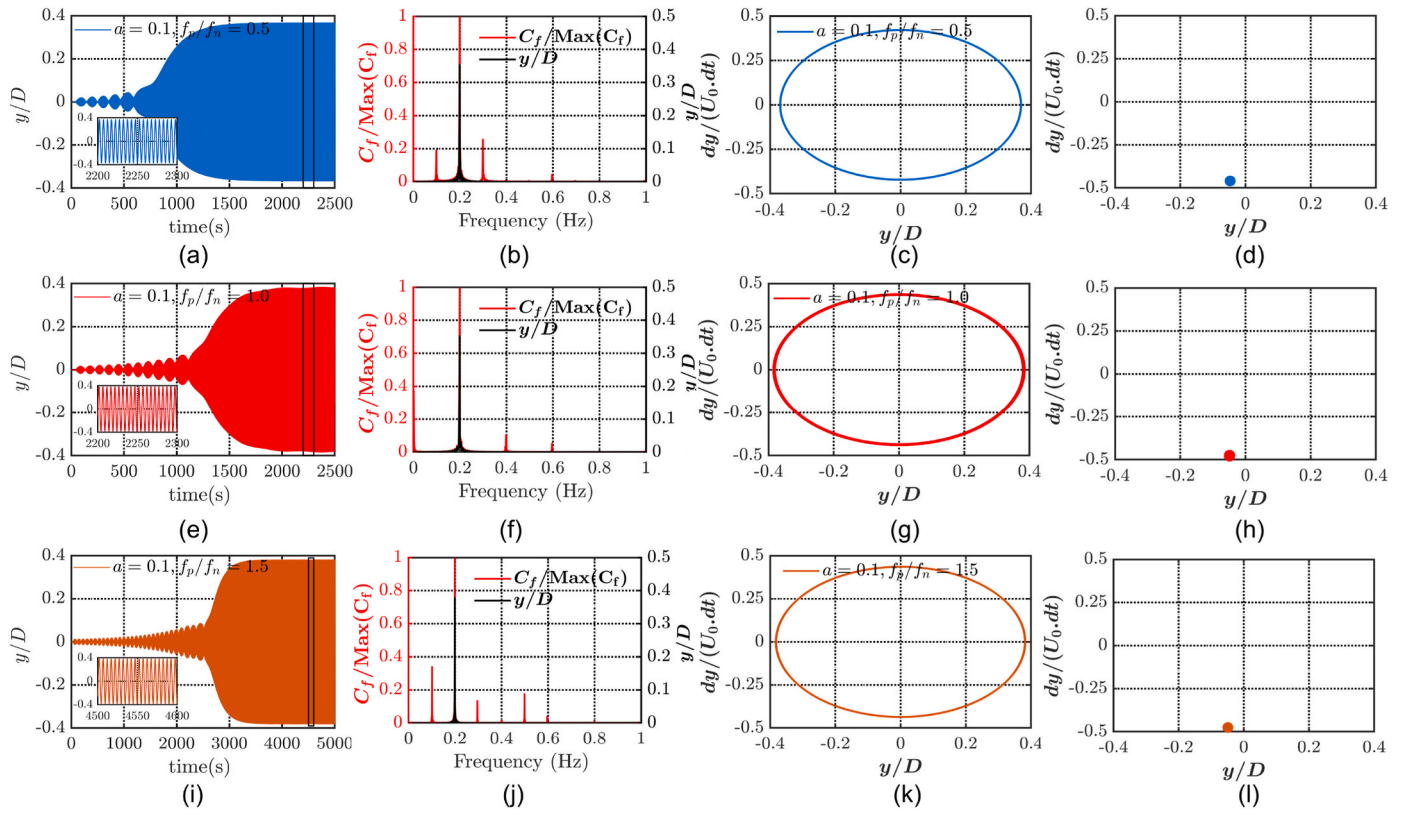
Fig. 6. Response of the circular cylinder with $a = 0.1$ and $f_p/f_n = [0.5, 1.0, 1.5]$: (a), (c), (i) time series; (b), (f), (j) frequency spectra; (c), (g), (k) phase portrait; and (d), (h), (l) Poincaré maps.
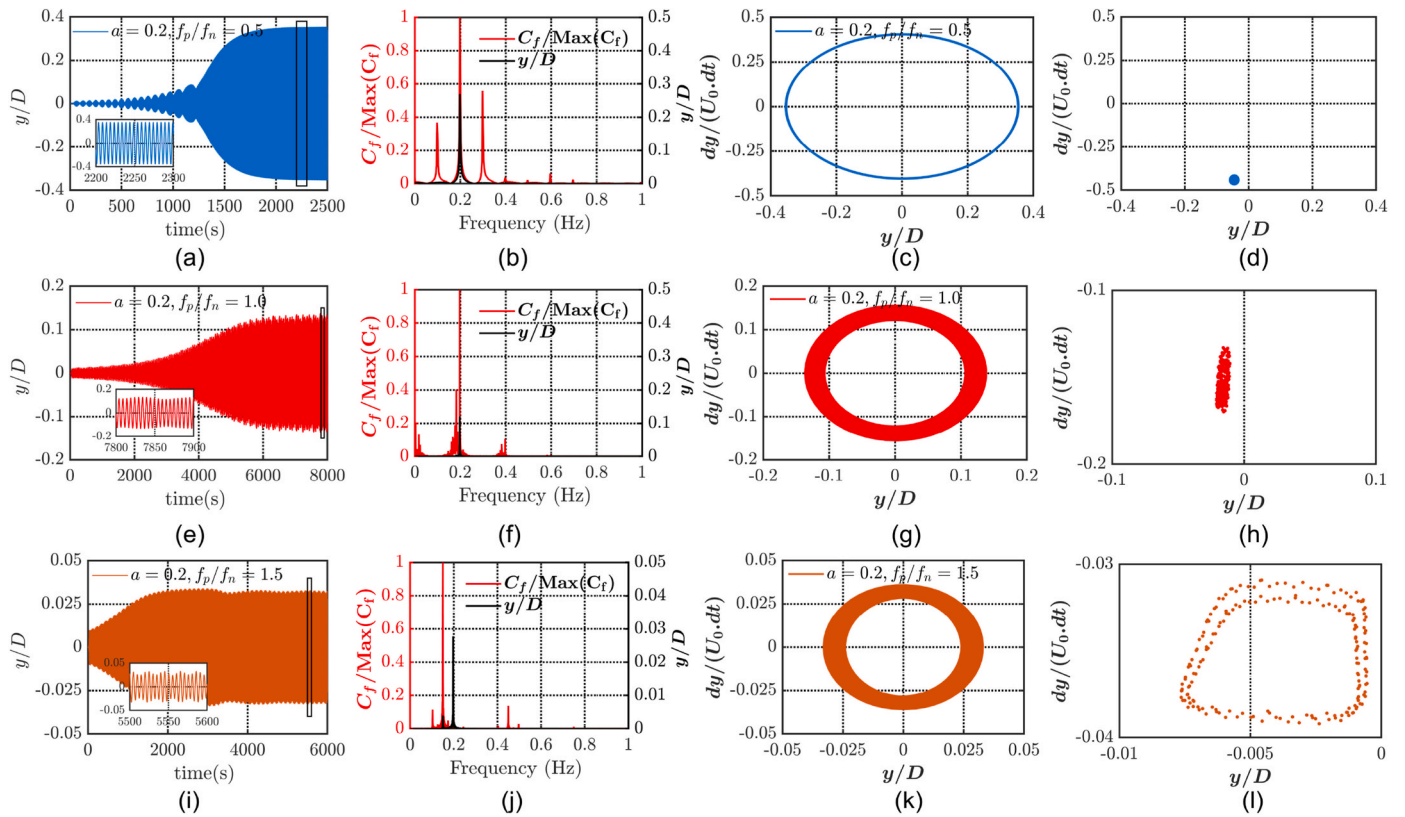
Fig. 7. Response of the circular cylinder with $a = 0.2$ and $f_p/f_n = [0.5, 1.0, 1.5]$: (a), (c), (i) time series; (b), (f), (j) frequency spectra; (c), (g), (k) phase portrait; and (d), (h), (l) Poincaré maps.
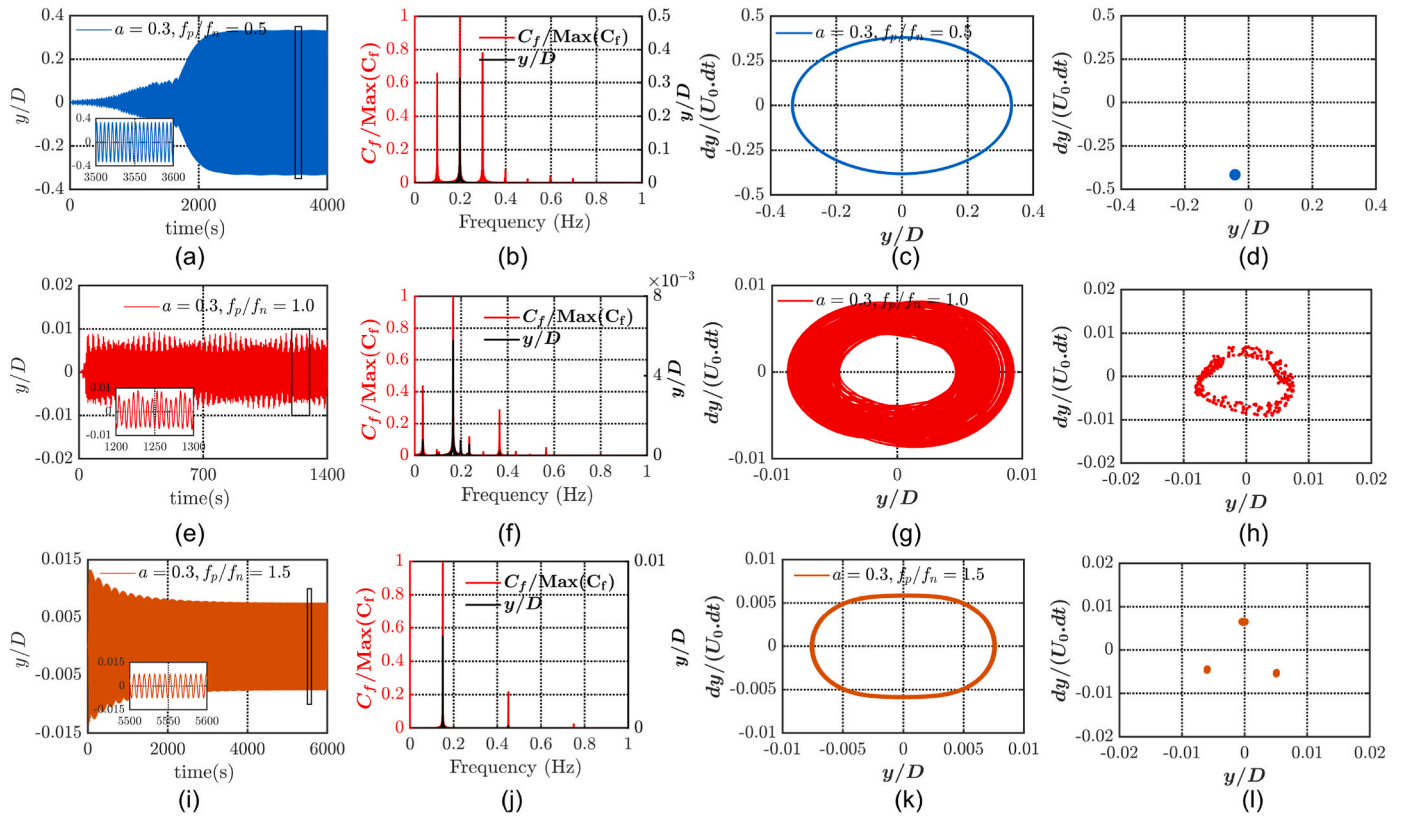
Fig. 8. Response of the circular cylinder with $a = 0.3$ and $f_p/f_n = [0.5, 1.0, 1.5]$: (a), (c), (i) time series; (b), (f), (j) frequency spectra; (c), (g), (k) phase portrait; and (d), (h), (l) Poincaré maps.
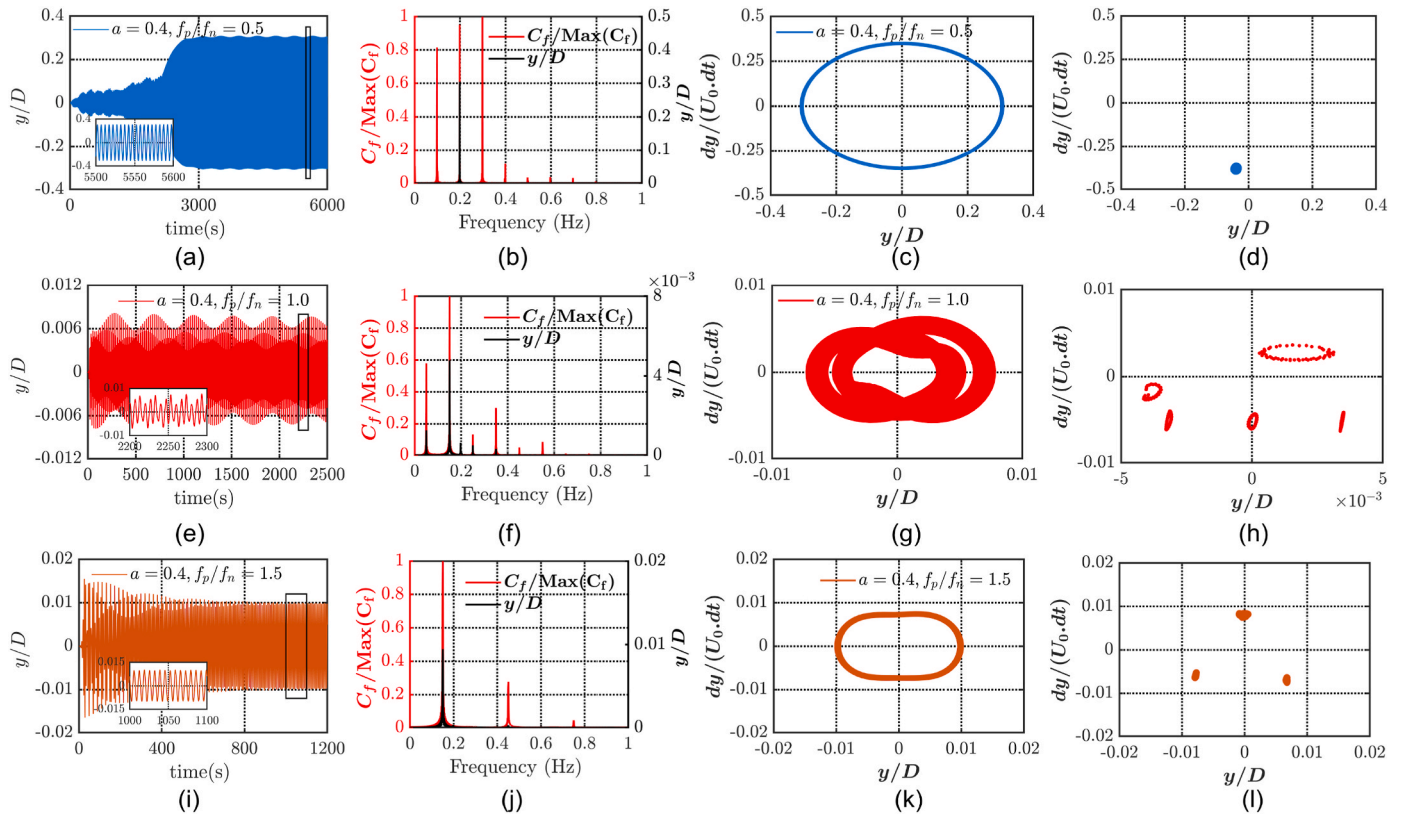
Fig. 9. Response of the circular cylinder with $a = 0.4$ and $f_p/f_n = [0.5, 1.0, 1.5]$: (a), (c), (i) time series; (b), (f), (j) frequency spectra; (c), (g), (k) phase portrait; and (d), (h), (l) Poincaré maps.
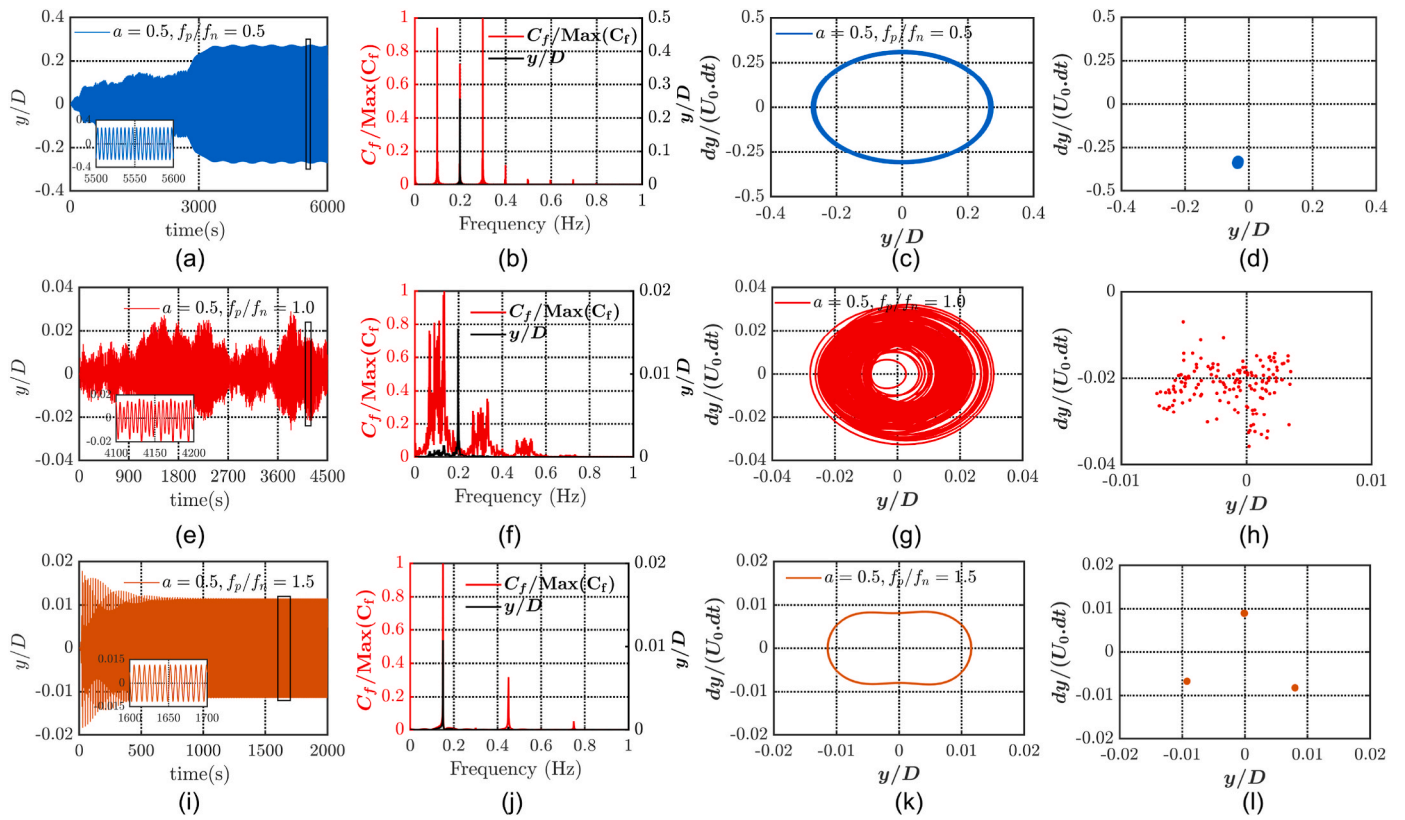
Fig. 10. Response of the circular cylinder with $a = 0.5$ and $f_p/f_n = [0.5, 1.0, 1.5]$: (a), (c), (i) time series; (b), (f), (j) frequency spectra; (c), (g), (k) phase portrait; and (d), (h), (l) Poincaré maps.

and 10(h)) suggests that the response of this system is quasi-periodic when $f_p/f_n = 1.0$. Additionally, there are three points shown in the Poincaré section, which demonstrate that the mechanical response of this coupled system is triple-periodic with $a = 0.3 - 0.5$ as f_p/f_n is increased to 1.5 (see Figs. 8(l)-10(l)), although the amplitude is negligible.

Based on the results presented above, we find that the response of cylinder is periodic when $a = 0.1$ and f_p/f_n ranges from 0.5 to 1.5, or when $f_p/f_n = 0.5$ and a ranges from 0.2 to 0.5. When $f_p/f_n = 1.0$, the vortex induced vibration of this coupled system exhibits more complex dynamic behavior with the increase of a. These findings suggest that the mechanical behavior of the system is highly dependent on a and f_p/f_n.

The phase difference $\Delta\varphi$ between the lift force F_L and the vibration displacement y can provide a more intuitive description of the state of vibration and the excitation mechanism of the circular cylinder. Table 1 shows the variation of the phase difference $\Delta\varphi$ of this oscillating system with different a and f_p/f_n. It can be seen that $\Delta\varphi$ is always larger than 0. This indicates that the structure captures energy from the pulsating flow which increases the amplitude of the cylinder. However, the phase difference is far from 0 within the "lock in" range, which implies that the

vibration of the cylinder and the vortex shedding are not completely synchronized. This is due to the fact that the interaction between VIV and excitation of pulsating flow leads to a nonlinear response of the vibration system. Moreover, we find that $\Delta\varphi$ is close to 0 when the response of the cylinder is quasi-periodic or triple-periodic. This reveals that the vibration of the cylinder and the vortex shedding are almost synchronized. However, the amplitude is more than two orders of magnitude lower than the amplitude within "lock in" range (see Figs. 8–10). This is mainly because that the cylinder vibrates at f_s, deviating from the natural frequency f_n, which is not able to induce resonance.

In order to properly analyze the characteristics of the vortex shedding under pulsating flow, we assess the vorticity contours of three different cases with distinct response characteristics. The evolutions of vorticity within an oscillation cycle are shown in Fig. 11, where the initial position of the cylinder marked as dotted line is used to recognize the displacement of the cylinder. We observe that the alternate shedding of a pair of vortices within a transverse oscillation cycle occurs as shown in Fig. 11(a) for $a = 0.1, f_p/f_n = 0.5$, which implies that the wake mode is '2 S'. The wake is in a pattern of two rows of vortex pairs. We also observe that the pattern of the vortex shedding shown in Fig. 11(a) is very similar to that of the oscillating cylinder under the constant inflow. The vortices intensity is weakened as vortices move downstream. Further, a pair of vortices and a single vortex are found to be shed alternately from the cylinder in one entire cycle as shown in Fig. 11(b) for $a = 0.4, f_p/f_n = 1.0$. The associated wake mode is 'T', which is defined as a wake mode where the flow switches between two modes alternately. In this case, it switches from '2 S' to 'S'. The displacement of the vibration has a beating feature (see Fig. 9(e)), which validates this wake mode 'T'. The wake mode shown in Fig. 11(c) for $a = 0.5, f_p/f_n = 1.5$ is also '2 S'. However, it can be noted that the space between neighboring vortices becomes larger than that shown in Fig. 11(a). Additionally, a pair of vortices diverges as the they flow downstream.

Table 1
Phase difference between the lift-force and the vibration displacement under pulsating flow.

f_p/f_n	a				
	0.1	0.2	0.3	0.4	0.5
0.5	$\Delta\varphi = 52.96°$	$\Delta\varphi = 56.79°$	$\Delta\varphi = 60.93°$	$\Delta\varphi = 67.96°$	$\Delta\varphi = 78.51°$
1.0	$\Delta\varphi = 47.75°$	$\Delta\varphi = 10.68°$	$\Delta\varphi = 0.654°$	$\Delta\varphi = 0.386°$	$\Delta\varphi = 8.981°$
1.5	$\Delta\varphi = 51.71°$	$\Delta\varphi = 9.734°$	$\Delta\varphi = 0.371°$	$\Delta\varphi = 0.373°$	$\Delta\varphi = 0.367°$
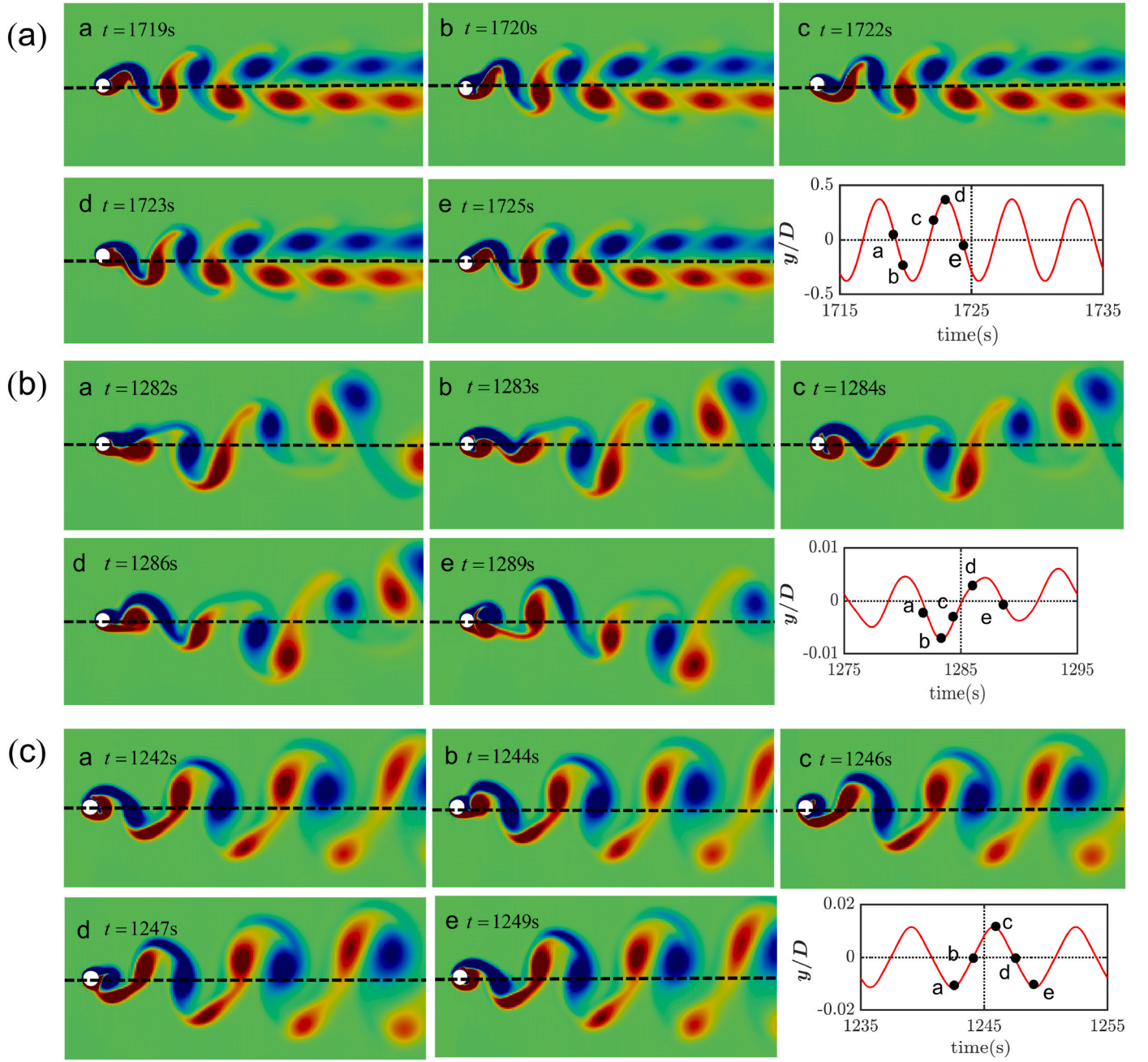
Fig. 11. Vorticity fields within an oscillation cycle with different a and f_p/f_n: (a) $a = 0.1, f_p/f_n = 0.5$, (b) $a = 0.4, f_p/f_n = 1.0$ (c) $a = 0.5, f_p/f_n = 1.5$.

4. Transverse galloping of a square cylinder

The equation of motion of the transverse galloping for a square cylinder is expressed as

$$m\ddot{y} + c\dot{y} + ky = F_y(t) \tag{6}$$

where F_y is the force per unit length of the square cylinder in the transverse direction, $F_y = \rho^f \; U^2 \; D \; C_y/2$. The fluid force F_y is evaluated by taking the quasi-steady (QS) assumption (Barrero-Gil et al., 2009). Here, C_y is the fluid flow transverse force coefficient which can be expressed as an odd series expansion of an angle of incidence $\alpha \approx \dot{y}/U$ for relatively small α. According to (Luo et al., 2003), a fifth-order polynomial can fit the C_y versus α at low Re very well. Therefore, using the fifth-order polynomial for C_y, and introducing dimensionless time and space coordinates, $\tau = \omega_n t$ and $\eta = y/D$, respectively, the

dimensionless equation of motion can be written as

$$\ddot{\eta} + (2\zeta - \lambda U_R a_1)\dot{\eta} - \frac{\lambda a_3}{U_R}(\dot{\eta})^3 - \frac{\lambda a_5}{(U_R)^3}(\dot{\eta})^5 + \eta = 0 \tag{7}$$

where ζ is the structural damping ratio of the square cylinder structure, the reduced velocity $U_R = U/\omega_n D$, λ is a dimensionless mass ratio, $\lambda = \rho D^2/2m$. Coefficients a_j are taken from (Sohankar et al., 1998).

We consider the square cylinder problem set up such that the Reynolds number is 250 for the baseline case of constant inflow velocity. The parameters of interest for the pulsating flow are $a \in [0.1, 0.5]$ and $f_p/f_n \in [0.5, 1.5]$. Nonlinear equation Eq. (7) is solved using the 4th-order Runge-Kutta method. The initial conditions are given by $\eta = 0$, and $\dot{\eta}$ is set to 0.000001 as the initial disturbance. We compare the results of QS model and FSI simulations, highlighting the limitations of the former, and present comprehensive results of FSI simulations of galloping of the

square for different parameters.

4.1. Results and discussion

The FSI simulation result is in good agreement with that of the QS model for the constant flow case, as shown in Fig. 12(a). The oscillation frequency $f_v = 0.059$ Hz and the shedding frequency $f_s = 0.4$ Hz are distinct, as expected in galloping, as shown in Fig. 12(b). The normalized amplitude A/D, oscillation frequency ratio f_v/f_n and vortex shedding frequency ratio f_s/f_n obtained with the FSI solver are in good agreement with other simulated results (Kadapa et al., 2017; Kadapa, 2020; Dettmer and Perić, 2006; He et al., 2014), as shown in Table 2.

Next, galloping of the square under pulsating flow are discussed. The amplitudes of the square obtained for pulsating flow conditions shown in Fig. 13 illustrate that the amplitude obtained by the QS model shows significant variation with frequency ratio f_p/f_n compared to the FSI simulated results. This observation suggests that this model fails to capture the response of the square cylinder in pulsating flow accurately, which necessitates the use of FSI simulations to determine response characteristics for these problems which are highly nonlinear.

The amplitude spectra of the displacement of the square cylinder with pulsating flow are as presented in Fig. 14, where eleven different spectra for $f_p/f_n \in [0.5, 1.5]$ are shown for $a = \{0.1, 0.2, 0.3, 0.4, 0.5\}$. The vibration amplitudes of the structure are also marked with red dots. It can be observed that every spectrum at different a and f_p/f_n has only one dominant peak value. The frequency with the highest peak in the spectrum is defined as the primary peak frequency, while the frequency corresponding to the secondary peak is defined as the secondary peak frequency. The red lines connected by the amplitudes of the primary peak frequencies are approximately parallel to the x-axis, and all primary peak frequencies of the vibration shown in Fig. 14 are close to $f_n \approx 0.06$ Hz. Therefore, the results depicted in Fig. 15 reveal that a and f_p/f_n do not have a significant influence on the primary vibration frequency of galloping of the square cylinder. In addition, it is observed that multiple vibration frequencies occur around the primary peak frequencies when f_p/f_n is between 1.1 and 1.3 for $a \in [0.1, 0.3]$, indicating that the vibration is irregular. Furthermore, we can see that the amplitude of the secondary peak frequency becomes larger as a increases.

From the variations of the amplitude of the structure for different pulsating flow parameters shown in Fig. 15, we observe that fluctuations in the amplitude as f_p/f_n increases from 0.5 to 1.5. Moreover, it evident that the peak vibration amplitude is typically observed when the frequency ratio is approximately 1.0, with the exception of $a = 0.5$, where the variation of the amplitude is more pronounced as the frequency ratio varies. Additionally, it can be noted that the maximum of the amplitude rises as a increases.

To further understand the galloping responses of a square cylinder with pulsating flow, we select several typical cases and plot the time

Table 2
Simulated results of galloping of the square cylinder at Re = 250 with a = 0.

Study	f_v/f_n	f_s/f_n	A/D
Dettmer and Perić (Dettmer and Perić, 2006)	0.943	6.33	1.117
Kadapa et al. (Kadapa et al., 2017)	0.944	–	1.197
Kadapa (Kadapa, 2020)	0.939	6.488	1.174
He et al. (He et al., 2014)	0.939	6.525	1.159
Present	0.949	6.484	1.194
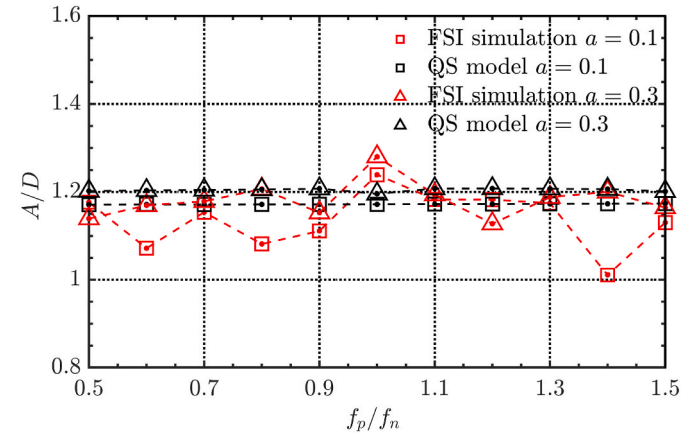
Fig. 13. Comparison of non-dimensional amplitude of square cylinder from FSI simulations and the quasi-steady model at Re = 250 under pulsating flow.

series of the displacement and contours of time-frequency. The non-dimensional displacement for a square cylinder with time at different a and f_p/f_n are shown in Fig. 16. In the case of $a = 0.1$, the repeatability of the vibration can be observed. Meanwhile, the square cylinder vibrates predominantly in a single frequency (see Fig. 16(a)). As f_p/f_n is increased to 1.0, the vibration slightly varies from one period to another. Further, the mean position of the cylinder slightly biases upwards during some periods (see Fig. 16(b)). In the case of $a = 0.3$ and $a = 0.5$, we also observed that the galloping is not symmetric and the mean position of a cylinder biases more significantly upward and downward for some periods (see Fig. 16(e) and (h)). The beating phenomenon (see Fig. 16(d), (f), (g) and (i)) indicates that there are more than one frequency components in vibration. The irregularity of the vibration is more obvious when f_p/f_n is 0.5 or 1.5.

We also employ the Morlet wavelet to analyze the vibration frequency and observe that the square cylinder vibrates at f_v which is in the vicinity of the natural frequency for different a and f_p/f_n. When $a = 0.1$ and $f_p/f_n = 0.5$, the vibration is regular and stable (see Fig. 17(a)). When
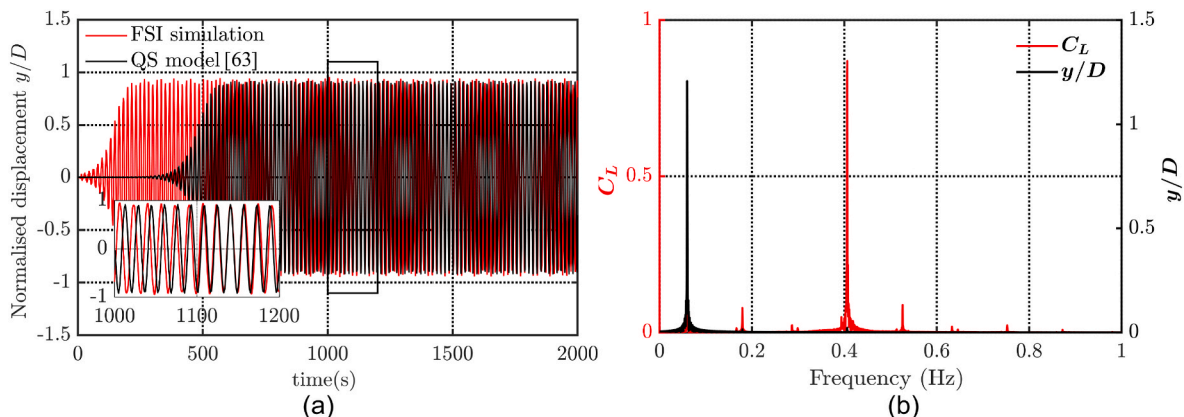
Fig. 12. Comparison of displacement of square cylinder for Re = 250 with $a = 0$: (a) displacement versus time, (b) frequency spectra.
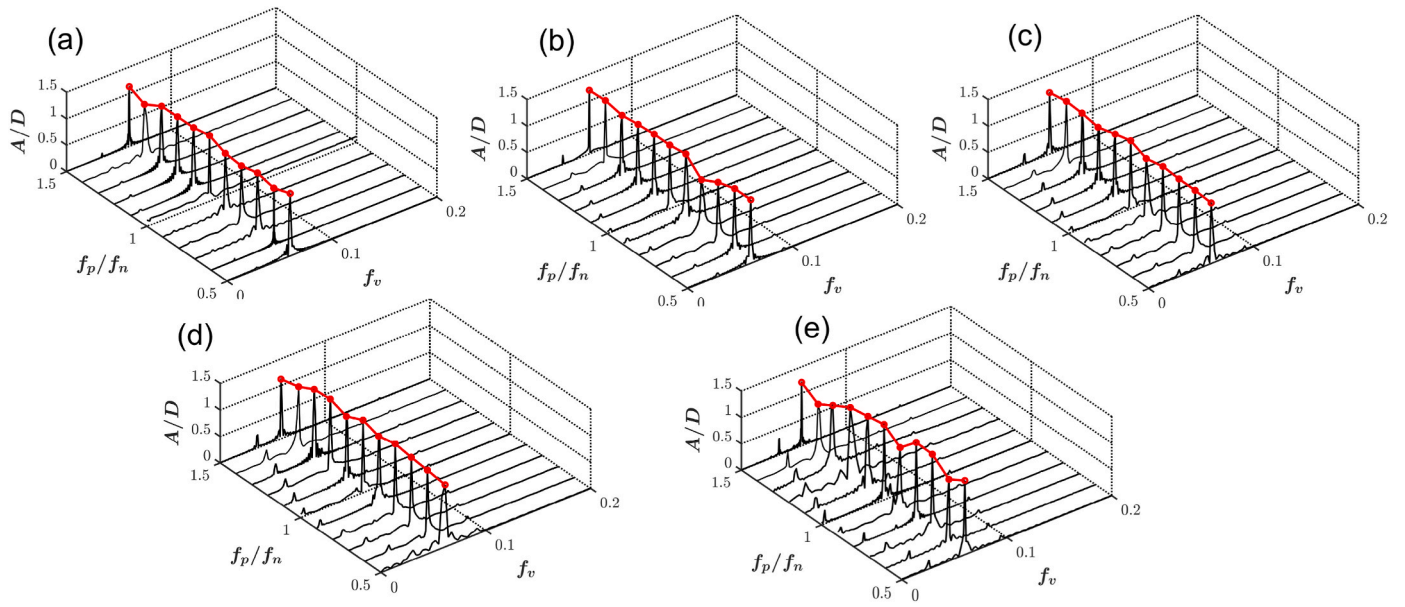
Fig. 14. The normalized amplitude predicted by FSI simulations with different a over the range $0.5 \le f_p/f_n \le 1.5$: (a) $a = 0.1$, (b) $a = 0.2$, (c) $a = 0.3$, (d) $a = 0.4$, (e) $a = 0.5$.
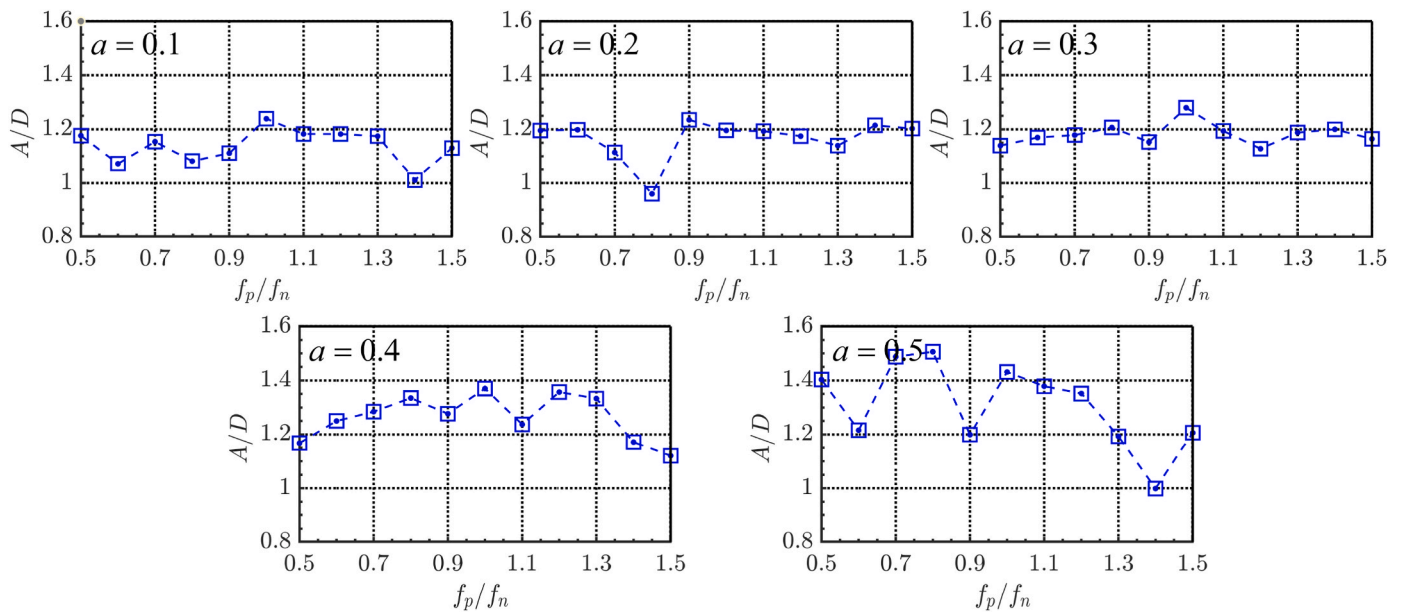
Fig. 15. Amplitude variations with respect to the frequency ratio f_p/f_n under different a.

$f_p/f_n = 1.0$, the amplitude of peak frequency increases gradually over time and then decreases for some period, after which the pattern repeats with another gradual increase and subsequent decrease in amplitude (see Fig. 17(b)). Additionally, the peak vibration frequency exhibits a more pronounced periodic pattern as a increases (see Fig. 17(f) and (i)). Moreover, the periodic pattern can be better demonstrated by the time series of displacement (see Fig. 17(b), (e) and (h)). It is noted from Fig. 17(c) that the vibration frequency of the square cylinder includes a low frequency when $a = 0.1$ and $f_p/f_n = 1.5$. Furthermore, with the increase of a, the amplitude of the low frequency is larger than that of $a = 0.1$ when the frequency ratio is 0.5 or 1.5. In addition, the occurrence of the low frequency verifies the beating phenomenon discussed previously (see Fig. 16). The vibration of the square cylinder becomes more irregular as a and f_p/f_n reaches their maximum (see Fig. 17(g) and (j)).

The correlation between the vibration frequency and the number of vortices shed during each period is examined through the wake visualizations as shown in Figs. 18 and 19. The lift coefficient exhibits a periodic pattern with a certain number of oscillations during each period of the displacement under the pulsating flow. This indicates that the square cylinder is undergoing fully developed galloping. Further, the amplitude of the lift coefficient exhibits a positive correlation with the pulsating inlet velocity U.

A total of 16 vortices are formed in each oscillation period, with an 8 P pattern (see Fig. 18(a)). Specifically, the 16 vortices observed consist of eight pairs, with four pairs shed during the falling process and the remaining four pairs shed during the rising process of galloping. Furthermore, it can be observed that the eight cycles of the lift coefficient within one period of the square cylinder vibration correspond to the shedding of eight vortices pairs. It can be observed from Fig. 18(a)
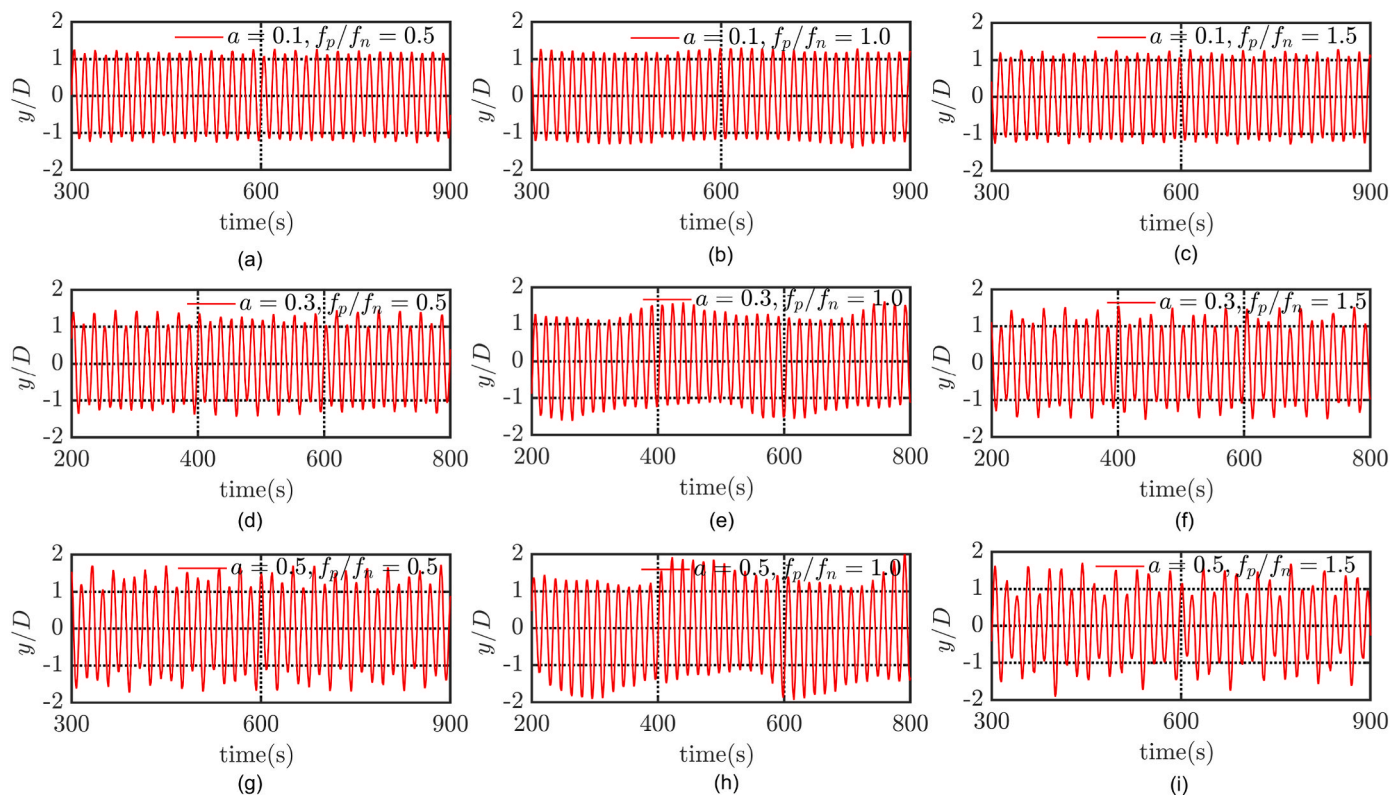
Fig. 16. Time series of the displacement of the square at $Re = 250$ for different a and f_p/f_n.

that vortex A is shed when the cylinder is at its lowest position. Vortices B–D are shed from the cylinder as the cylinder moves from its lowest position to its initial position. Moreover, as the vortices move downstream, the wake pattern of the square cylinder exhibits the splitting and combination of vortices. Since the splitting and merging of the vortices occur far downstream of the cylinder, they do not have a significant impact on vortex shedding. When $f_p/f_n = 1.5$, the wake pattern is similar to that of the oscillating square cylinder with $f_p/f_n = 0.5$ (see Fig. 18(c)). In each oscillation period, a total of 14 vortices are formed, with a 6 P + 2 S wake mode when $f_p/f_n = 1.0$ (see Fig. 18(b)). Two single vortices are generated when the square cylinder moves to the highest and lowest locations. When the cylinder moves upwards and downwards, the vortex shedding frequency increases. During the rising and falling processes of the square cylinder, the remaining 12 vortices form six pairs that are shed from the cylinder. Compared with the vortices shown in Fig. 18(a) and (c), the vortices become larger. Further, we can observe that in a pair of vortices, both the positive and negative ones are split into two, and these split vortices move faster than the neighboring pair of vortices downstream. Subsequently, they merge with the positive and negative vortices of a neighboring pair of vortices, respectively, as they continue to move downstream.

Subsequently, the time series in Fig. 19 indicates that in each period of displacement, the number of periodic oscillations in the lift coefficient is lower, and the amplitude of the lift coefficient is larger when compared to the case of $a = 0.1$. A total of 12 vortices are formed in each oscillation period, with a 6 P pattern for different f_p/f_n (see Fig. 19). Compared with the wake pattern shown in Fig. 18(a), the splitting and merging of two neighboring pairs of vortices give rise to a more complex vortex dynamic, characterized by nonlinear behavior and interactions (see Fig. 19(a)). It is worth noting that the splitting and merging of vortices occur near the upstream of the structure as f_p/f_n is increased (see Fig. 19(b) and (c)). Therefore, the splitting and merging of vortices have significant influences on vortex shedding. We observe that the size of the vortices shed is inconsistent and the spacing between vortices is

greater than that in other cases as f_p/f_n increases to 1.5. Several pairs of vortices show a divergent trend in both upper right and lower right directions as they move downstream (see Fig. 19(c)). This phenomenon is mainly attributed to the interaction between the upstream and downstream vortices, which can cause an increase in instability and result in the formation of more complex vortex structures.

5. Conclusions

We investigated VIV of a circular cylinder and galloping of a square cylinder in pulsating inflow conditions using a FSI simulation framework. From FSI simulations, we observe that the vibration response of VIV varies significantly with different values of a and f_p/f_n. We have identified the unique dynamic response characteristics of the coupled system, including periodic, quasi-periodic, and chaotic responses. Meanwhile, the observed phenomenon of the pulsating flow suppressing VIV of the cylinder can be attributed to the fact that the vibration frequency of the cylinder is influenced by the pulsating flow, which in turn prevents synchronization from occurring. To the best of our knowledge, the galloping of a square cylinder under pulsating flow has been investigated here for the first time. In this study, we observe that the gradually increasing parameter a leads to an increasing trend in amplitude and a more pronounced increase in the amplitude of the response. Moreover, distinct vibration features can be observed in the time-frequency domain of the vibration amplitude with different frequency ratios f_p/f_n, Additionally, the vortex shedding structure exhibits instability and high nonlinearity as a and f_p/f_n increase.

We have established that the standard wake oscillator model is insufficient in explaining the phenomenon where the structure jumps out of the "lock in" region at a fixed Reynolds number due to the variation of the frequency ratio of pulsating flow. Regarding galloping, the quasi-steady model is insufficient to capture the beating characteristics and other highly nonlinear displacement response characteristics of the square cylinder in pulsating flow, as it neglects the effects of unsteady
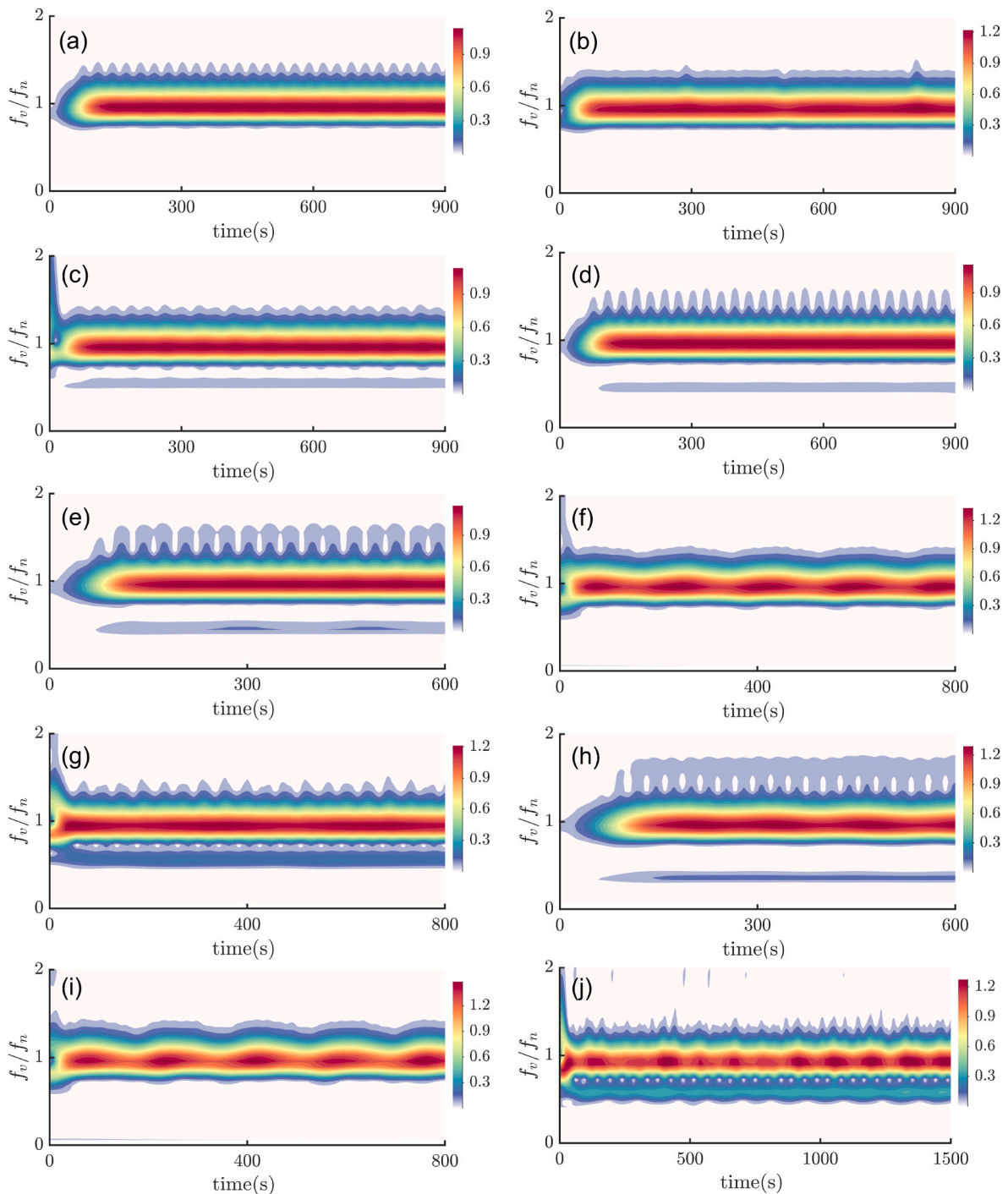
Fig. 17. Contours of the vibration amplitude in the time-frequency domain: (a) $a = 0.1, f_p/f_n = 0.5$, (b) $a = 0.1, f_p/f_n = 1.0$, (c) $a = 0.1, f_p/f_n = 1.5$, (d) $a = 0.2, f_p/f_n = 0.5$, (e) $a = 0.3, f_p/f_n = 0.5$, (f) $a = 0.3, f_p/f_n = 1.0$, (g) $a = 0.3, f_p/f_n = 1.5$, (h) $a = 0.4, f_p/f_n = 0.5$, (i) $a = 0.4, f_p/f_n = 1.0$, (j) $a = 0.5, f_p/f_n = 1.5$.

flow on the galloping motion. The significance of the research discussed above allows us to identify potential areas for future work. We plan to enhance the accuracy of wake oscillator and quasi-steady models by including physical coupled terms and harmonic forces that account for the unsteady vortex shedding forces, which will enable us to capture the behavior of flow-induced vibration in pulsating flow with greater accuracy (Joly et al., 2012; Han et al., 2021).

In our FSI simulations, we have only considered the response of circular and square cylinders at a fixed Reynolds number for different values of amplitude and frequency of pulsating inflow. In future investigations, we plan to extend this study to a selected range of Reynolds

numbers, including turbulence regime. This will help to gain a better understanding of the parameters that play a critical role in suppressing or attenuating flow induced vibrations of bluff bodies.
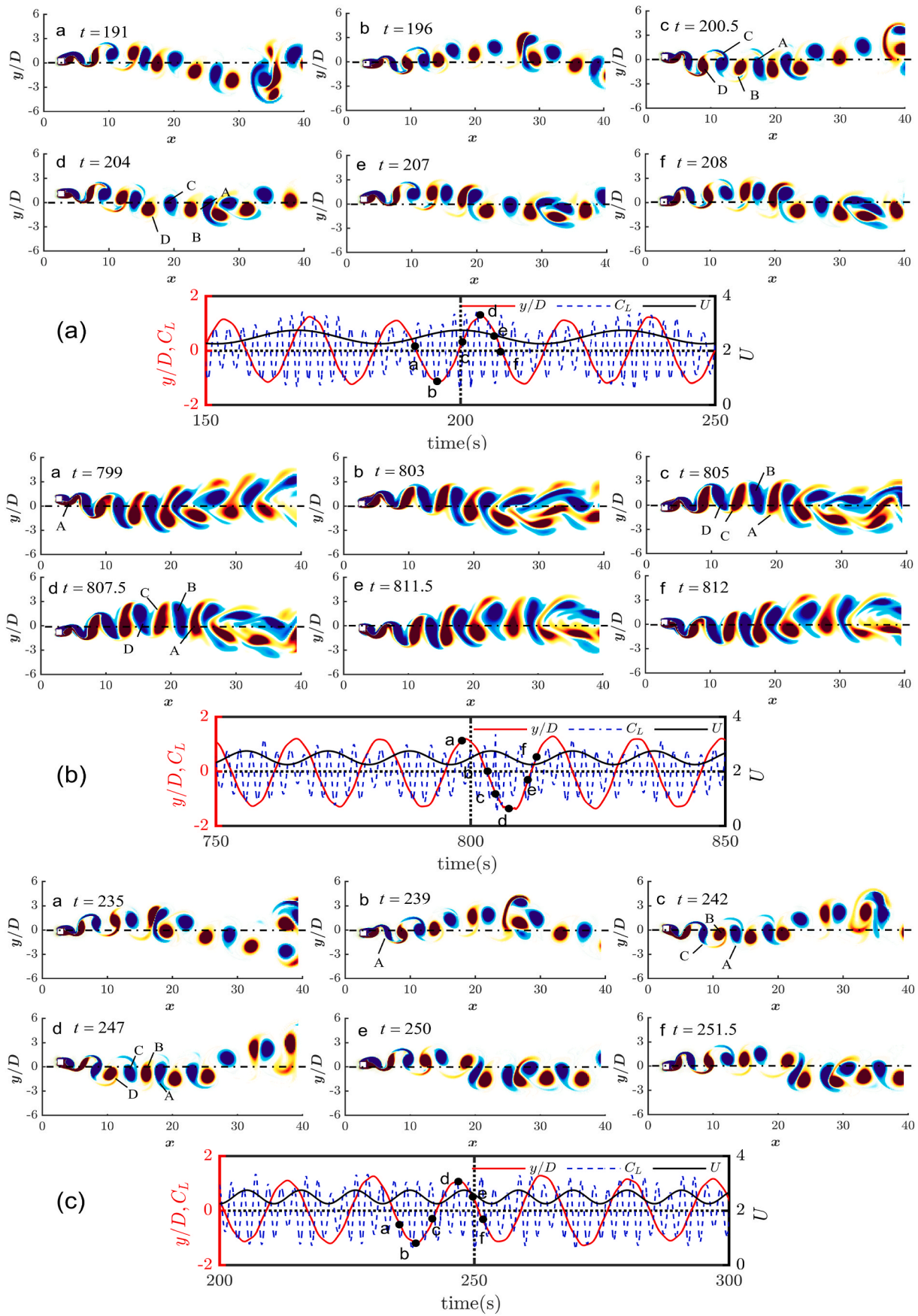
Fig. 18. Vorticity contours for $a = 0.1$ at different f_p/f_n: (a) $f_p/f_n = 0.5$, (b) $f_p/f_n = 1.0$, (c) $f_p/f_n = 1.5$.
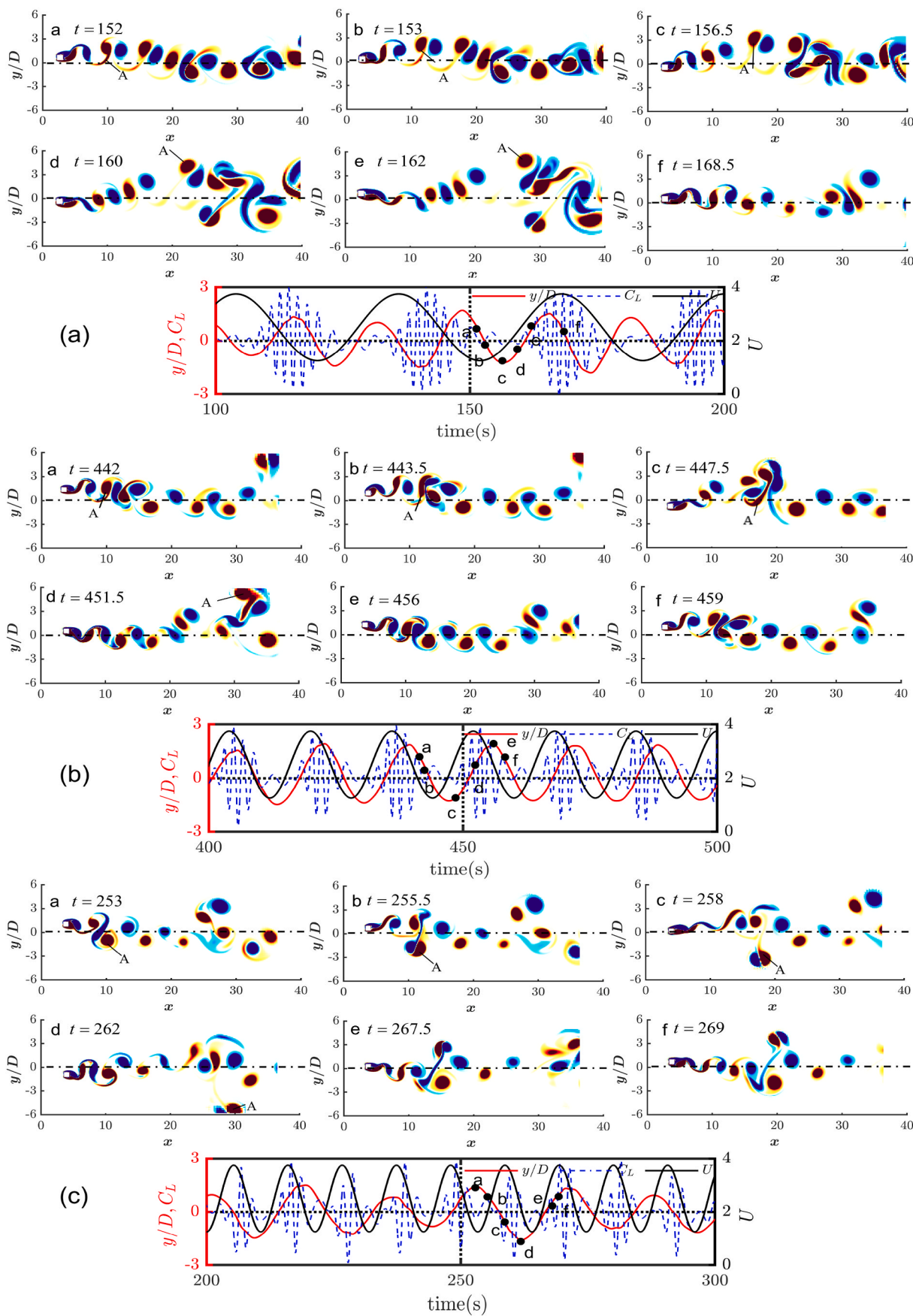
Fig. 19. Vorticity contours for $a = 0.5$ at different f_p/f_n: (a) $f_p/f_n = 0.5$,(b) $f_p/f_n = 1.0$, (c) $f_p/f_n = 1.5$.

CRediT authorship contribution statement

Xinyu Wang: Writing – original draft, Visualization, Validation, Software, Methodology, Investigation. **Zhongliang Zhang:** Visualization, Validation, Software, Resources. **Kai Shi:** Writing – original draft, Visualization, Software, Resources, Data curation. **Xuefeng Zhu:** Software, Investigation, Data curation. **Xu Guo:** Supervision, Resources. **Yue Mei:** Writing – review & editing, Writing – original draft, Supervision, Investigation, Conceptualization. **Chennakesava Kadapa:** Writing – review & editing, Writing – original draft, Validation, Supervision, Software, Conceptualization.

Declaration of competing interest

The authors declare that they have no known competing financial interests or personal relationships that could have appeared to influence the work reported in this paper.

Data availability

Data will be made available on request.

References

Abdelkefi, A., Hajj, M.R., Nayfeh, A.H., 2012. Power harvesting from transverse galloping of square cylinder. Nonlinear Dynam. 70, 1355–1363. https://doi.org/10.1007/s11071-012-0538-4.

Alonso, G., Meseguer, J., 2006. A parametric study of the galloping stability of two-dimensional triangular cross-section bodies. J. Wind Eng. Ind. Aerod. 94, 241–253. https://doi.org/10.1016/j.jweia.2006.01.009.

An, H., Cheng, L., Zhao, M., 2009. Steady streaming around a circular cylinder in an oscillatory flow. Ocean Eng. 36, 1089–1097. https://doi.org/10.1016/j.oceaneng.2009.06.010.

Anagnostopoulos, P., Iliadis, G., 1998. Numerical study of the flow pattern and the in-line response of a flexible cylinder in an oscillating stream. J. Fluid Struct. 12, 225–258. https://doi.org/10.1006/jfls.1997.0139.

Andrianne, T., Aryoputro, R.P., Laurent, P., Colson, G., Amandolèse, X., Hémon, P., 2018. Energy harvesting from different aeroelastic instabilities of a square cylinder. J. Wind Eng. Ind. Aerod. 172, 164–169. https://doi.org/10.1016/j.jweia.2017.10.031.

Armin, M., Khorasanchi, M., Day, S., 2018. Wake interference of two identical oscillating cylinders in tandem: an experimental study. Ocean Eng. 166, 311–323. https://doi.org/10.1016/j.oceaneng.2018.08.012.

Barrero-Gil, A., Sanz-Andrés, A., Roura, M., 2009. Transverse galloping at low Reynolds numbers. J. Fluid Struct. 25, 1236–1242. https://doi.org/10.1016/j.jfluidstructs.2009.07.001.

Bearman, P.W., 1984. Vortex shedding from oscillating bluff bodies. Annu. Rev. Fluid Mech. 16, 195–222. https://doi.org/10.1146/annurev.fl.16.010184.001211.

Bearman, P.W., Downie, M.J., Graham, J.M.R., Obasaju, E.D., 1985. Forces on cylinders in viscous oscillatory flow at low Keulegan-Carpenter numbers. J. Fluid Mech. 154, 337–356. https://doi.org/10.1017/S0022112085001562.

Bearman, P.W., Gartshore, I.S., Maull, D.J., Parkinson, G.V., 1987. Experiments on flow-induced vibration of a square-section cylinder. J. Fluid Struct. 1, 19–34. https://doi.org/10.1016/S0889-9746(87)90158-7.

Blevins, R.D., 1990. Flow-induced Vibration. Van Nostrand Reinhold, Washington, DC.

Bokaian, A., Geoola, F., 1984. Wake-induced galloping of two interfering circular cylinders. J. Fluid Mech. 146, 383–415. https://doi.org/10.1017/S0022112084001920.

Bornemann, P.B., Cirak, F., 2013. A subdivision-based implementation of the hierarchical b-spline finite element method. Comput. Methods Appl. Mech. Eng. 253, 584–598. https://doi.org/10.1016/j.cma.2012.06.023.

Burman, E., Claus, S., Hansbo, P., Larson, M.G., Massing, A., 2015. CutFEM: discretizing geometry and partial differential equations. Int. J. Numer. Methods Eng. 104, 472–501. https://doi.org/10.1002/nme.4823.

Cavaglieri, D., Bewley, T., 2015. Low-storage implicit/explicit Runge–Kutta schemes for the simulation of stiff high-dimensional ODE systems. J. Comput. Phys. 286, 172–193. https://doi.org/10.1016/j.jcp.2015.01.031.

Daqaq, M.F., Alhadidi, A.H., Khazaaleh, S., 2022. Suppression of structural galloping by applying a harmonic base excitation at certain frequencies. Nonlinear Dynam. 110, 3001–3014. https://doi.org/10.1007/s11071-022-07815-7.

Derakhshandeh, J.F., Arjomandi, M., Dally, B., Cazzolato, B., 2016. Flow-induced vibration of an elastically mounted airfoil under the influence of the wake of a circular cylinder. Exp. Therm. Fluid Sci. 74, 58–72. https://doi.org/10.1016/j.expthermflusci.2015.12.003.

Dettmer, W., Perić, D., 2006. A computational framework for fluid–rigid body interaction: finite element formulation and applications. Comput. Methods Appl. Mech. Eng. 195, 1633–1666. https://doi.org/10.1016/j.cma.2005.05.033.

Dettmer, W.G., Perić, D., 2013. A new staggered scheme for fluid–structure interaction. Int. J. Numer. Methods Eng. 93, 1–22. https://doi.org/10.1002/nme.4370.

Dettmer, W.G., Kadapa, C., Perić, D., 2016. A stabilised immersed boundary method on hierarchical b-spline grids. Comput. Methods Appl. Mech. Eng. 311, 415–437. https://doi.org/10.1016/j.cma.2016.08.027.

Dettmer, W.G., Lovrić, A., Kadapa, C., Perić, D., 2021. New iterative and staggered solution schemes for incompressible fluid-structure interaction based on Dirichlet-Neumann coupling. Int. J. Numer. Methods Eng. 122, 5204–5235. https://doi.org/10.1002/nme.6494.

Facchinetti, M.L., de Langre, E., Biolley, F., 2004. Coupling of structure and wake oscillators in vortex-induced vibrations. J. Fluid Struct. 19, 123–140. https://doi.org/10.1016/j.jfluidstructs.2003.12.004.

Gao, C., Shi, Z., Zhang, W., 2023. Data-knowledge-driven semi-empirical model augmentation method for nonlinear vortex-induced vibration. Nonlinear Dynam. 111, 20617–20642. https://doi.org/10.1007/s11071-023-08966-x.

Guo, H., Liu, B., Yu, Y., Cao, S., Chen, Y., 2017. Galloping suppression of a suspended cable with wind loading by a nonlinear energy sink. Arch. Appl. Mech. 87, 1007–1018. https://doi.org/10.1007/s00419-017-1227-z.

Han, P., de Langre, E., 2022. There is no critical mass ratio for galloping of a square cylinder under flow. J. Fluid Mech. 931, A27 https://doi.org/10.1017/jfm.2021.975.

Han, P., Hémon, P., Pan, G., de Langre, E., 2021. Nonlinear modeling of combined galloping and vortex-induced vibration of square sections under flow. Nonlinear Dynam. 103, 3113–3125.

He, T., Zhou, D., Han, Z., Tu, J., Ma, J., 2014. Partitioned subiterative coupling schemes for aeroelasticity using combined interface boundary condition method. Int. J. Comput. Fluid Dynam. 28, 272–300. https://doi.org/10.1080/10618562.2014.927057.

Jafari, M., Hou, F., Abdelkefi, A., 2020. Wind-induced vibration of structural cables. Nonlinear Dynam. 100, 351–421. https://doi.org/10.1007/s11071-020-05541-6.

Jansen, K.E., Whiting, C.H., Hulbert, G.M., 2000. A generalized-α method for integrating the filtered Navier–Stokes equations with a stabilized finite element method. Comput. Methods Appl. Mech. Eng. 190, 305–319. https://doi.org/10.1016/S0045-7825(00)00203-6.

Jauvtis, N., Williamson, C.H.K., 2004. The effect of two degrees of freedom on vortex-induced vibration at low mass and damping. J. Fluid Mech. 509, 23–62. https://doi.org/10.1017/S0022112004008778.

Joly, A., Etienne, S., Pelletier, D., 2012. Galloping of square cylinders in cross-flow at low Reynolds numbers. J. Fluid Struct. 28, 232–243. https://doi.org/10.1016/j.jfluidstructs.2011.12.004.

Kadapa, C., 2020. A second-order accurate non-intrusive staggered scheme for the interaction of ultra-lightweight rigid bodies with fluid flow. Ocean Eng. 217, 107940 https://doi.org/10.1016/j.oceaneng.2020.107940.

Kadapa, C., 2022. A unified simulation framework for fluid–structure–control interaction problems with rigid and flexible structures. Int. J. Comput. Methods 19, 2150052. https://doi.org/10.1142/s0219876221500523.

Kadapa, C., Dettmer, W.G., Perić, D., 2017. A stabilised immersed boundary method on hierarchical b-spline grids for fluid–rigid body interaction with solid–solid contact. Comput. Methods Appl. Mech. Eng. 318, 242–269. https://doi.org/10.1016/j.cma.2017.01.024.

Kadapa, C., Dettmer, W.G., Perić, D., 2018. A stabilised immersed framework on hierarchical b-spline grids for fluid-flexible structure interaction with solid–solid contact. Comput. Methods Appl. Mech. Eng. 335, 472–489. https://doi.org/10.1016/j.cma.2018.02.021.

Kadapa, C., Dettmer, W.G., Perić, D., 2020. Accurate iteration-free mixed-stabilised formulation for laminar incompressible Navier–Stokes: applications to fluid–structure interaction. J. Fluid Struct. 97, 103077 https://doi.org/10.1016/j.jfluidstructs.2020.103077.

Kadapa, C., Wang, X., Mei, Y., 2022. A comprehensive assessment of accuracy of adaptive integration of cut cells for laminar fluid-structure interaction problems. Comput. Math. Appl. 122, 1–18. https://doi.org/10.1016/j.camwa.2022.07.006.

Kazakevich, M.I., Vasilenko, A.G., 1996. Closed analytical solution for galloping aeroelastic self-oscillations. J. Wind Eng. Ind. Aerod. 65, 353–360. https://doi.org/10.1016/S0167-6105(97)00053-6.

Khalak, A., Williamson, C.H.K., 1997. Investigation of relative effects of mass and damping in vortex-induced vibration of a circular cylinder. J. Wind Eng. Ind. Aerod. 69–71, 341–350. https://doi.org/10.1016/S0167-6105(97)00167-0.

Li, T., Zhang, J., Zhang, W., 2011. Nonlinear characteristics of vortex-induced vibration at low Reynolds number. Commun. Nonlinear Sci. Numer. Simulat. 16, 2753–2771. https://doi.org/10.1016/j.cnsns.2010.10.014.

Luo, S.C., Chew, Y.T., Ng, Y.T., 2003. Hysteresis phenomenon in the galloping oscillation of a square cylinder. J. Fluid Struct. 18, 103–118. https://doi.org/10.1016/S0889-9746(03)00084-7.

Martins, F.A.C., Avila, J.P.J., 2019. Effects of the Reynolds number and structural damping on vortex-induced vibrations of elastically-mounted rigid cylinder. Int. J. Mech. Sci. 156, 235–249. https://doi.org/10.1016/j.ijmecsci.2019.03.024.

Menon, K., Mittal, R., 2019. Flow physics and dynamics of flow-induced pitch oscillations of an airfoil. J. Fluid Mech. 877, 582–613. https://doi.org/10.1017/jfm.2019.627.

Modi, V.J., Welt, F., Seto, M.L., 1995. Control of wind-induced instabilities through application of nutation dampers: a brief overview. Eng. Struct. 17, 626–638. https://doi.org/10.1016/0141-0296(95)00033-4.

Parkinson, G.V., 1974. Mathematical Models of Flow-Induced Vibrations of Bluff Bodies. Karlsruhe, Germany.

Parkinson, G.V., Smith, J.D., 1964. The square prism as an aeroelastic non-linear oscillator. Q. J. Mech. Appl. Math. 17, 225–239. https://doi.org/10.1093/qjmam/17.2.225.

Plaschko, P., 2000. Global chaos in flow-induced oscillations of cylinders. J. Fluid Struct. 14, 883–893. https://doi.org/10.1006/jfls.2000.0298.

Prasanth, T.K., Mittal, S., 2008. Vortex-induced vibrations of a circular cylinder at low Reynolds numbers. J. Fluid Mech. 594, 463–491. https://doi.org/10.1017/S0022112007009202.

Qi, X., Dai, S., Ren, C., Dong, Q., Xiong, C., 2023. Numerical simulation of flow-induced vibration of a circular cylinder close to a free surface at low Reynolds number. Phys. Fluids 35. https://doi.org/10.1063/5.0132674.

Qiu, T., Lin, W., Du, X., Zhao, Y., 2021. Mass ratio effect on vortex-induced vibration for two tandem square cylinders at a low Reynolds number. Phys. Fluids 33. https://doi.org/10.1063/5.0070603.

Roshko, A., 1952. On the Development of Turbulent Wakes From Vortex Streets. California Institute of Technology. https://doi.org/10.7907/4WDN-9807.

Rüberg, T., Cirak, F., 2014. A fixed-grid b-spline finite element technique for fluid–structure interaction. Int. J. Numer. Methods Fluid. 74, 623–660. https://doi.org/10.1002/fld.3864.

Sarpkaya, T., 2004. A critical review of the intrinsic nature of vortex-induced vibrations. J. Fluid Struct. 19, 389–447. https://doi.org/10.1016/j.jfluidstructs.2004.02.005.

Skop, R.A., Balasubramanian, S., 1997. A new twist on an old model for vortex-excited vibrations. J. Fluid Struct. 11, 395–412. https://doi.org/10.1006/jfls.1997.0085.

Sohankar, A., Norberg, C., Davidson, L., 1998. Low-Reynolds-number flow around a square cylinder at incidence: study of blockage, onset of vortex shedding and outlet boundary condition. Int. J. Numer. Methods Fluid. 26, 39–56. https://doi.org/10.1002/(SICI)1097-0363(19980115)26:1<39::AID-FLD623>3.0.CO;2-P.

Tezduyar, T.E., Senga, M., 2006. Stabilization and shock-capturing parameters in SUPG formulation of compressible flows. Comput. Methods Appl. Mech. Eng. 195, 1621–1632. https://doi.org/10.1016/j.cma.2005.05.032.

Tezduyar, T.E., Mittal, S., Ray, S.E., Shih, R., 1992. Incompressible flow computations with stabilized bilinear and linear equal-order-interpolation velocity-pressure elements. Comput. Methods Appl. Mech. Eng. 95, 221–242. https://doi.org/10.1016/0045-7825(92)90141-6.

Tian, H., Shan, X., Li, X., Wang, J., 2023a. Enhanced airfoil-based flutter piezoelectric energy harvester via coupling magnetic force. Appl. Energy 340, 120979. https://doi.org/10.1016/j.apenergy.2023.120979.

Tian, H., Shan, X., Wang, H., Li, X., Su, Y., Wang, J., 2023b. Enhanced piezoelectric energy harvesting performance using trailing-edge flap. Ocean Eng. 285, 115443 https://doi.org/10.1016/j.oceaneng.2023.115443.

Wang, J., Sheng, L., Ding, L., 2023. A comprehensive numerical study on flow-induced vibrations with various groove structures: suppression or enhancing energy scavenging. Ocean Eng. 271, 113781 https://doi.org/10.1016/j.oceaneng.2023.113781.

Weaver, D.S., Fitzpatrick, J.A., 1988. A review of cross-flow induced vibrations in heat exchanger tube arrays. J. Fluid Struct. 2, 73–93. https://doi.org/10.1016/S0889-9746(88)90137-5.

Williamson, C.H.K., Govardhan, R., 2008. A brief review of recent results in vortex-induced vibrations. J. Wind Eng. Ind. Aerod. 96, 713–735. https://doi.org/10.1016/j.jweia.2007.06.019.

Zhang, M., Zhang, C., Abdelkefi, A., Yu, H., Gaidai, O., Qin, X., Zhu, H., Wang, J., 2021. Piezoelectric energy harvesting from vortex-induced vibration of a circular cylinder: effect of Reynolds number. Ocean Eng. 235, 109378 https://doi.org/10.1016/j.oceaneng.2021.109378.

Zhao, M., Cheng, L., An, H., 2012. Numerical investigation of vortex-induced vibration of a circular cylinder in transverse direction in oscillatory flow. Ocean Eng. 41, 39–52. https://doi.org/10.1016/j.oceaneng.2011.12.017.

Zhao, M., Kaja, K., Xiang, Y., Yan, G., 2013. Vortex-induced vibration (VIV) of a circular cylinder in combined steady and oscillatory flow. Ocean Eng. 73, 83–95. https://doi.org/10.1016/j.oceaneng.2013.08.006.

Zhao, M., Cheng, L., An, H., Lu, L., 2014. Three-dimensional numerical simulation of vortex-induced vibration of an elastically mounted rigid circular cylinder in steady current. J. Fluid Struct. 50, 292–311. https://doi.org/10.1016/j.jfluidstructs.2014.05.016.